ATOMIC PARITY NONCONSERVATION EXPERIMENTS

E.N. FORTSON

University of Washington, Seattle, WA 98195, USA

and

L.L. LEWIS

National Bureau of Standards, Boulder, CO 80303, USA

NORTH-HOLLAND PHYSICS PUBLISHING–AMSTERDAM

PHYSICS REPORTS (Review Section of Physics Letters) 113, No. 5 (1984) 289–344. North-Holland, Amsterdam

ATOMIC PARITY NONCONSERVATION EXPERIMENTS

E.N. FORTSON

University of Washington, Seattle, WA 98195, USA

and

L.L. LEWIS

National Bureau of Standards, Boulder, CO 80303, USA

Received March 1984

Contents:

Abstract:

A comprehensive review of theoretical and experimental studies of parity nonconservation in atoms is presented. We describe measurements in bismuth, lead, cesium, and thallium which collectively provide confirmation of the Weinberg–Salam–Glashow "standard model" of electroweak unification. Ongoing experiments in hydrogen are discussed as well. We examine the unique role of all atomic experiments in distinguishing alternative versions of the standard theory. Finally, we include some discussion of experiments which search for permanent atomic electric dipole moments as potential evidence of time-reversal violation in particle interaction.

1. Introduction

Physicists used to believe that parity is conserved in all interactions, and that natural laws do not distinguish between the left and the right. The discovery in 1956 that parity is not conserved [1, 2] had an immediate and profound influence on nuclear and elementary particle physics. However, there was no such sudden impact on atomic physics because the force that distinguishes between the left and the right, the weak interaction, is dwarfed in comparison with the electric and magnetic forces in atoms. There is no atomic process, as in nuclear β decay, in which the weak interaction is uniquely manifested. Only recently, over two decades after the original parity revolution, has parity nonconservation (PNC) finally been observed in the electronic structure of atoms.

Atomic PNC is caused by an interesting form of the weak interaction not known in 1956, the neutral current form in which the interacting particles (electrons and nucleons in the case of atoms) do not change charge. These weak neutral currents are a central prediction of the unified theory of weak and electromagnetic forces developed by Glashow [3], Weinberg [4], Salam [5], and others in the 1960's. One of the important tests of this theory has been to find the expected effects of the neutral current interaction in atoms. Now that these effects have been observed, atomic PNC measurements should continue to play a useful role in working toward a complete understanding of weak neutral currents.

An important symmetry that characterizes the unified theory in its present form is time-reversal invariance (T-symmetry). Likewise, the observed atomic PNC effects, such as optical rotation, possess T-symmetry. A different type of PNC effect that violates T-symmetry is a permanent atomic electric dipole moment (EDM) aligned with the atom's angular momentum. Although no such EDM has yet been found it has been sought in neutrons [6] and in atoms and molecules [7]. If detected, an EDM would confirm the long suspected existence of T-violating forces between elementary particles. We will include some discussion of this important topic, while reserving the bulk of the review for the experiments that have actually observed atomic PNC, and their interpretation in terms of weak neutral currents.

A number of reviews [8] have previously appeared on the subject of atomic parity nonconservation, but the major issues have since become clarified by additional experimental work. We believe it is time for a new comprehensive review of the entire field.

1.1. Neutral current weak interaction and gauge theories

As early as 1959 Zel'dovich [9] estimated the size of optical rotation due to a neutral current form of the weak interaction that might be expected in a gas of ground state atomic hydrogen and concluded that this particular effect would be far too small to observe. Later Curtis-Michel [10] analyzed some possible experiments with excited states of hydrogen which would take advantage of the close proximity of states of opposite parity, but at that time the experiments still seemed to be very difficult.

Two serious attempts [11] were made in the 1960's to observe PNC in atomic systems by looking for circular polarization associated with magnetic-dipole transitions. Upper limits were set for molecular oxygen and atomic lead, but neither experiment approached the sensitivity required to observe weak interaction effects.

Meanwhile, extraordinary advances in the field theory of weak interactions during the 1960's strengthened the theoretical basis for weak neutral currents. Renormalizable gauge theories of the interactions among elementary particles led to a unified picture of the weak and electromagnetic forces. The simplest of these theories was that of Weinberg [4] and Salam [5], often called the "standard

model" of electro-weak interactions, in which the weak interaction between any pair of fermions is mediated by the exchange of massive vector bosons, two charged ones, $W^{\pm}$, and one neutral one, Z^0. Only one free parameter is introduced, the mixing angle between the bare Z^0 and bare photon, called the Weinberg angle, θ_w.

The charged bosons mediate the familiar form of weak interaction known in the earlier language of current–current interaction as the charged (or perhaps better, charge-changing) current process. The best known example is ordinary β decay, in which a neutron is converted into a proton while an antineutrino and an electron are created, i.e. $n \rightarrow p + e + \tilde{\nu}$. The equivalent scattering process is $n + \nu \rightarrow p + e$. In both cases the neutron–proton current acts through a $W^{\pm}$ with the neutrino–electron current.

The weak neutral currents predicted by the Weinberg–Salam theory are mediated by the neutral Z^0. In the case of atoms, this neutral current allows the direct first-order weak interaction of the atomic electrons with the nucleons and with each other without changing the atom's identity. For example, $e + p \rightarrow e + p$, $e + n \rightarrow e + n$, and also $e + e \rightarrow e + e$. In these cases, the electron–electron current acts through the Z^0 with either the proton–proton, neutron–neutron, or electron–electron current.

In 1973 high energy neutrino–nucleon scattering experiments [12] demonstrated the existence of such weak neutral currents in nature. A variety of experiments have subsequently shown neutral current phenomena, all consistent with predictions of the Weinberg–Salam theory. The PNC neutral current interaction between electrons and nucleons has been established both by measurements of high energy inelastic electron scattering from protons and deuterons [13], and by the atomic PNC experiments to be discussed in this article. In addition, two groups using the CERN colliding beam facility have observed both the $W^{\pm}$ and the Z^0 resonances directly in proton–antiproton collisions [14].

1.2. Recent atomic parity nonconservation (PNC) experiments

Atomic PNC experiments under consideration in many laboratories received vital encouragement in 1974 when Bouchiat and Bouchiat [15] pointed out that there should be considerable enhancement of neutral current effects in heavy atoms. They showed that PNC effects should increase with atomic number Z roughly as Z^3, and demonstrated that the heavy atoms Cs and Tl should exhibit optical helicity more than 6 orders of magnitude greater than ground-state hydrogen. This work provided impetus to world-wide experimental efforts with Cs [15], Bi [7, 16, 17] and Tl [18]. Somewhat later, after attention was drawn [19] once again to experimental possibilities with metastable atomic hydrogen, a number of experiments to measure PNC in hydrogen also began [20–22].

After several years of intensive effort the original goal of detecting and studying weak neutral currents in atomic physics has been realized. Many experiments with heavy atoms have attained enough sensitivity to see PNC effects of the size expected. Over the same period the complex atomic calculations with heavy atoms have been refined considerably. All experimental results agree in sign, and most agree in approximate magnitude, with the predictions of the most recent atomic calculations using the Weinberg–Salam theory. However, there remain some discrepancies among the experimental results that need to be clarified, and we still await the first results from the important atomic hydrogen experiments. Improvements in all experiments are being implemented which should set more stringent limits on alternative gauge theories [23], detect certain neutral current couplings not yet observed [24], and possibly test the predicted contributions of Z^0 and $W^{\pm}$ radiative corrections [25].

There have also been recent limits set by experiments searching for a permanent atomic or molecular

EDM [26, 27], and new atomic EDM experiments have begun [28], with the goal of finding another manifestation of the *CP* violation observed long ago in K^0 decay [29].

2. Observable effects

2.1. PNC-induced electric dipole moments

The inversion symmetry of a physical system (and in a similar fashion the intrinsic symmetry of an elementary particle) can be described with the use of a parity operator, P. If the state function of the physical system is ψ, the operator P inverts the spatial coordinates of the function, so that $P\psi(\boldsymbol{r}) = \psi(-\boldsymbol{r})$. If $P\psi(\boldsymbol{r}) = \pm\psi(\boldsymbol{r})$, then we say that the function ψ has well defined parity (even parity if +, odd parity if −). We also say that parity is conserved by an interaction if the Hamiltonian, H, for that interaction commutes with the parity operator, or equivalently, if H is invariant under coordinate inversion.

The measured quantity in all atomic PNC experiments which search for the inversion asymmetry is an electric dipole moment $\mathscr{E}_{\mathrm{PNC}}$ induced in an atom by a force which violates parity conservation. When this force violates time-reversal symmetry as well, $\mathscr{E}_{\mathrm{PNC}}$ can be a permanent electric dipole moment (EDM) which causes an energy shift of the atom in an external electric field. If instead the force obeys time-reversal symmetry, $\mathscr{E}_{\mathrm{PNC}}$ is restricted to being a transition dipole moment which is observable through its interference with some other atomic moment in radiative transitions between atomic states.

We begin with a simplified discussion. First suppose there is a permanent electric dipole fixed parallel to the total atomic angular momentum $\boldsymbol{F}$ in a nondegenerate stationary state of an atom. In an external field $\boldsymbol{E}$ the energy shift $-\mathscr{E}_{\mathrm{PNC}} \cdot \boldsymbol{E}$, proportional to $\boldsymbol{F} \cdot \boldsymbol{E}$, clearly violates both P- and T-symmetry since $\boldsymbol{F} \to \boldsymbol{F}$, $\boldsymbol{E} \to -\boldsymbol{E}$ under P, while $\boldsymbol{F} \to -\boldsymbol{F}$, $\boldsymbol{E} \to \boldsymbol{E}$ under T. Thus an observation of a permanent EDM parallel to an atomic spin would be clear evidence of an interaction in the atom which violates time-reversal invariance. Next suppose that T-symmetry is not violated. Since we will observe no permanent electric dipole moment of the atom, how can we observe a PNC effect? We must look instead for oscillating dipole moments associated with transitions between atomic states. For example, suppose a magnetic dipole transition takes place with an oscillating atomic magnetic moment $\mathscr{M}$. The PNC force within the atom can induce $\mathscr{E}_{\mathrm{PNC}}$ with a component parallel to $\mathscr{M}$, but T-symmetry requires these two oscillating moments to differ in phase by $\pi/2$; otherwise the T-odd quantity $\mathscr{E}_{\mathrm{PNC}} \cdot \mathscr{M}$ would not average to zero. This phase difference in E1 and M1 radiation causes circular polarization, an observable PNC helicity effect in the case of time-reversal symmetry.

We now proceed to a complete and rigorous treatment. We consider a PNC force on the atomic electrons described by an operator H_{PNC}. In later sections we will discuss specific expressions for H_{PNC}, such as the interaction between electrons and nucleons predicted by the Weinberg–Salam–Glashow electro-weak theory. For now, H_{PNC} is any internal atomic operator that mixes electronic states of opposite parity.

To get an expression for the dipole moment, H_{PNC} is assumed small and treated only to first order in perturbation theory. Let $|k\rangle$ and E_k denote exact wave functions and energy eigenvalues in the absence of H_{PNC}, and let $|k_{\mathrm{PNC}}\rangle$ denote the wave function when H_{PNC} is included. Also let the electric dipole moment operator be $\boldsymbol{E}1 = -\Sigma\, e\boldsymbol{r}_i$ summed over electrons. Then

$$\mathscr{E}_{\mathrm{PNC}}(kj) \equiv \langle k_{\mathrm{PNC}}|\boldsymbol{E}1|j_{\mathrm{PNC}}\rangle = \sum_l \left\{ \frac{\langle k|H_{\mathrm{PNC}}|l\rangle\langle l|\boldsymbol{E}1|j\rangle}{E_k - E_l} + \frac{\langle k|\boldsymbol{E}1|l\rangle\langle l|H_{\mathrm{PNC}}|j\rangle}{E_j - E_l} \right\}. \tag{1}$$

The two terms in the sum represent perturbation by $H_{\rm PNC}$ of states k and j respectively. Note that for a nonzero value of $\mathcal{E}_{\rm PNC}(kj)$ the unperturbed states k and j must have the same parity since both $H_{\rm PNC}$ and $\boldsymbol{E}1$ are P-odd.

It is often useful to factor out the orientational dependence in eq. (1), that is, the dependence on initial and final magnetic quantum numbers m_j and m_k. We introduce a reduced matrix element $\mathcal{E}_{\rm PNC}(kj)$ defined by

$$\mathcal{E}_{\rm PNC}(kj)\,\hat{\boldsymbol{a}}(m_k m_j) = \boldsymbol{\mathcal{E}}_{\rm PNC}(kj) \tag{2}$$

where

$$\hat{\boldsymbol{a}}(m_k m_j) \equiv C_1(\hat{\boldsymbol{x}} \pm \mathrm{i}\hat{\boldsymbol{y}})\,\delta(m_k, m_j \pm 1) + C_0\hat{\boldsymbol{z}}\,\delta(m_k, m_j) \tag{3}$$

gives the orientational dependence, which is that of a vector operator [30], since $H_{\rm PNC}$ is a (pseudo-) scalar in terms of the total angular momentum. The Clebsch–Gordon coefficients C_1 and C_0 depend upon the initial and final angular momenta [30].

The usual convention is to choose the phases of the states to make the reduced matrix elements of $\langle k|\boldsymbol{E}1|l\rangle$ real. One can show [31] that with this convention the matrix elements of $H_{\rm PNC}$ are pure imaginary when $H_{\rm PNC}$ is even under T, and are real when $H_{\rm PNC}$ is odd under T. Using eq. (1) we then have:

$$\begin{aligned} &T\text{-symmetry:} && TH_{\rm PNC}T^{-1} = H_{\rm PNC}: && \boldsymbol{\mathcal{E}}_{\rm PNC}\ \text{imaginary} \\ &T\text{-violation:} && TH_{\rm PNC}T^{-1} = -H_{\rm PNC}: && \boldsymbol{\mathcal{E}}_{\rm PNC}\ \text{real}. \end{aligned} \tag{4}$$

As we have done above, we will often suppress the initial and final state indices on the dipole moments.

Since diagonal elements of $\boldsymbol{\mathcal{E}}_{\rm PNC}$ must be zero when it is pure imaginary, we see immediately that T-symmetry implies that there is no permanent electric dipole moment in a single atomic state, and therefore no shift in energy linear in an applied electric field. T-symmetry leads instead to the interference effects among transition moments discussed in the next section.

In the T-violating case there can be a permanent EDM in a nondegenerate stationary state k with an energy shift δE_k in an electric field $\boldsymbol{E}$:

$$\begin{aligned} &\delta E_k = -\boldsymbol{\mathcal{E}}_{\rm PNC}\cdot\boldsymbol{E} \\ &\boldsymbol{\mathcal{E}}_{\rm PNC} = 2\sum_l \frac{\langle k|H_{\rm PNC}|l\rangle\langle l|\Sigma_i\, e\boldsymbol{r}_i|k\rangle}{E_l - E_k}\ . \end{aligned} \tag{5}$$

We defer further discussion of the T-violation until section 7 where we will survey experiments designed to detect permanent EDM's in atoms and the limits they can set on possible T-violating interactions.

2.2. PNC-interference effects in atomic transitions

The PNC interaction of interest in most of this article exhibits time-reversal symmetry, and hence induces pure-imaginary atomic dipole moments that are observable in atomic transitions. There are two

important classes of such experiments, each involving the interference between an ordinary but relatively weak electromagnetic transition and the PNC-induced E1 transition. In the first (M1) class, $\mathscr{E}_{\rm PNC}$ is coupled into an M1 transition, producing circularly polarized light, or a rotation of plane polarized light. In the second (Stark) class of experiments, a static electric field $\boldsymbol{E}_{\rm s}$ induces an E1 transition between two states, which can interfere with the PNC-induced E1 transition between the same two states. The resultant transition rate depends on the relative directions of $\boldsymbol{E}_{\rm s}$ and the polarization vectors of the absorbed and re-emitted radiation in such a way as to manifest the violation of reflection symmetry just as the circular polarization does in the M1 experiments.

2.2.1. Circular dichroism and optical rotation

We now derive expressions for the circular dichroism and optical rotation that occur when a PNC-induced E1 transition between two states interferes with an M1 transition between the same two states. The M1 matrix element between two states is

$$\langle k_{\rm PNC}|\boldsymbol{M}1|j_{\rm PNC}\rangle \sim \langle k|\boldsymbol{M}1|j\rangle = -\frac{e\hbar}{2m_e c}\langle k|\boldsymbol{L}+2\boldsymbol{S}|j\rangle \equiv \mathscr{M}(kj)\,\hat{\boldsymbol{a}}(m_k m_j) \tag{6}$$

which vanishes unless the states k and j have the same parity. We have introduced a reduced matrix element, $\mathscr{M}(kj)$, following the model of eq. (2). (Again, we will often suppress the initial and final state indices.)

A circularly polarized electromagnetic wave travelling in the $\hat{z}$ direction has electric and magnetic field vectors:

$$\boldsymbol{E}_\eta = \frac{E_0}{\sqrt{2}}(\hat{\boldsymbol{x}} - \mathrm{i}\eta\hat{\boldsymbol{y}}), \qquad \boldsymbol{B}_\eta = \frac{B_0}{\sqrt{2}}(\mathrm{i}\eta\hat{\boldsymbol{x}} + \hat{\boldsymbol{y}}) \tag{7}$$

where $\eta = \pm 1$ gives the two states of circular polarization, the positive sign denoting right-hand circularly polarized light by the standard optical convention (which corresponds to negative helicity). Including both electric and magnetic dipole radiation between initial and final atomic states i and f, the transition amplitude is proportional to

$$A_\eta(\mathrm{fi}) = \langle \mathrm{f}_{\rm PNC}|(\boldsymbol{E}1\cdot\boldsymbol{E}_\eta + \boldsymbol{M}1\cdot\boldsymbol{B}_\eta)|\mathrm{i}_{\rm PNC}\rangle\,.$$

The circular polarization in emission is then given by

$$P_{\rm c} \equiv \sum_{m_{\rm f} m_{\rm i}} \frac{(|A_+|^2 - |A_-|^2)}{(|A_+|^2 + |A_-|^2)} = \frac{2\,\mathrm{Im}(\mathscr{E}_{\rm PNC}\mathscr{M})}{|\mathscr{E}_{\rm PNC}|^2 + |\mathscr{M}|^2} \sim 2\,\mathrm{Im}\left(\frac{\mathscr{E}_{\rm PNC}}{\mathscr{M}}\right), \tag{9}$$

where we have used eqs. (2), (3), (6), and (7), and in the last expression assumed $\mathscr{E}_{\rm PNC} \ll \mathscr{M}$.

Similarly, in the case of absorption, the absorptivity $\kappa_\pm$ will change between right and left circularly polarized light by a fractional amount 2δ, where

$$2\delta = (\kappa_+ - \kappa_-)/\kappa = 4\,\mathrm{Im}(\mathscr{E}_{\rm PNC}/\mathscr{M})\,. \tag{10}$$

δ is called the circular dichroism, and we have assumed $\kappa \sim \kappa_+ \sim \kappa_-$, implying $\delta \ll 1$. Because of

experimental limitations, the present atomic experiments do not attempt to measure either P_c or δ directly, but rather make use of techniques which increase signal through interference with a Stark-induced transition, as discussed in section 2.2.3.

Any substance which exhibits circular dichroism must also demonstrate optical activity. This feature is a result of the difference in the real part of the refractive index $n_\pm$ for right and left circularly polarized light. From dispersion relations we have

$$(n_+ - n_-)/(n-1) = (\kappa_+ - \kappa_-)/\kappa\,, \tag{11}$$

where $n \sim n_+ \sim n_-$. Because of the differing phase velocities $c/n_\pm$, the polarization plane of linearly polarized light of wavelength λ will be rotated in a distance l by an angle

$$\phi = \frac{\pi l}{\lambda}(n_+ - n_-) = \frac{4\pi l}{\lambda}(n-1)\,\mathrm{Im}\,\frac{\mathscr{E}_{\mathrm{PNC}}}{\mathscr{M}} = \frac{4\pi l}{\lambda}(n-1)R\,, \qquad R \equiv \mathrm{Im}(\mathscr{E}_{\mathrm{PNC}}/\mathscr{M}) \tag{12}$$

where we have used the optical convention in which the rotation is considered positive when it appears clockwise to an observer looking into the source.

Note that the angle ϕ follows the dispersive line shape of $(n-1)$ which is always a useful discriminant against spurious rotations. Such PNC optical rotation is the object of experiments made by groups at Seattle, Oxford, Novosibirsk and Moscow.

2.2.2. Comparison with a helical antenna

For a physical picture of the effects discussed above, a simple analogy may be drawn between the PNC circular dichroism of an atom and that of a helical antenna which is small compared to the radiation wavelength. Charge moving in the antenna produces E1 and M1 moments parallel to the axis of the helix, proportional respectively to the charge displacement $q = q_0 \exp(\mathrm{i}\omega t)$ along the axis and to the current $I = \dot{q} = q_0\omega \exp\{\mathrm{i}(\omega t + \pi/2)\}$ about the axis. These moments have a relative phase difference of $\pi/2$. The radiated electric and magnetic field components in the plane of the axis thus also differ in phase by $\pi/2$, which means the radiation has partial circular polarization $2|\mathscr{E}|\,|\mathscr{M}|/(|\mathscr{E}|^2 + |\mathscr{M}|^2)$. Conversely, there is a circular polarization dependence associated with absorption of radiation by the antenna.

Introducing a parity-nonconserving term $\sim \boldsymbol{\sigma}\cdot\boldsymbol{\rho}$ in the electronic Hamiltonian similarly creates a handedness or screw sense in the atom. Classically, a radiating electronic orbit becomes helical with the axis of the helix aligned normal to the change in angular momentum. Note that the screw sense of a helix is invariant with respect to rotation by π about an axis normal to the helix axis. Therefore, the circular dichroism is independent of the relative orientations of several atoms in a sample. The E1 and M1 amplitudes that result from the helical motion differ in phase by $\pi/2$, just as in the simple antenna above. This phase difference, obvious in the case of the antenna, is guaranteed by T-invariance as previously noted.

2.2.3. PNC-Stark interference

In the second class of experiments the PNC-induced E1 moment interferes with a Stark-induced E1 moment instead of an M1 moment. When an external static electric field $\boldsymbol{E}_s$ is applied to the atom, a

Stark E1 amplitude $\mathscr{E}_s$ appears with a form similar to the PNC amplitude in eq. (1).

$$\mathscr{E}_s(kj) = \langle k_s|\boldsymbol{E}1|j_s\rangle = e^2 \sum_l \left\{ \frac{\langle k|\boldsymbol{r}|l\rangle\langle l|\boldsymbol{E}_s\cdot\boldsymbol{r}|j\rangle}{E_k - E_l} + \frac{\langle k|\boldsymbol{E}_s\cdot\boldsymbol{r}|l\rangle\langle l|\boldsymbol{r}|j\rangle}{E_j - E_l} \right\}, \tag{13}$$

where the Stark perturbed states are given a subscript s, and we use j and k for initial and final states.

For analyzing the geometry of experiments, it is helpful to use the vector $\hat{\boldsymbol{a}}$ defined in eq. (3);

$$\langle k_s|\boldsymbol{E}1|j_s\rangle = e^2 \sum_l r_{kl} r_{lj} \left\{ \frac{\hat{\boldsymbol{a}}(m_k m_l)\,\boldsymbol{E}_s\cdot\hat{\boldsymbol{a}}(m_l m_j)}{E_k - E_l} + \frac{\boldsymbol{E}_s\cdot\hat{\boldsymbol{a}}(m_k m_l)\,\hat{\boldsymbol{a}}(m_l m_j)}{E_j - E_l} \right\}, \tag{14}$$

where $\langle k|\boldsymbol{r}|l\rangle = \hat{\boldsymbol{a}}(m_k m_l) r_{kl}$.

The Stark-PNC form of interference is utilized in experiments with heavy atoms at Berkeley and Paris, and in many experiments with hydrogen. We defer to a later section the discussion of hydrogen. Here we present a qualitative sketch of the scheme used at Paris and Berkeley. The basic idea, originally pointed out by Bouchiat and Bouchiat [32], is that an electronic polarization (i.e. a nonzero expectation value of the electronic angular momentum $\langle \boldsymbol{J}\rangle$) in the excited state of the atom is induced by absorption of a circularly polarized photon directed perpendicular to an applied static electric field.

For definiteness, let the static electric field be in the x direction, $\boldsymbol{E}_s = E_s\hat{\boldsymbol{x}}$, and let the incident photon have its momentum $\boldsymbol{k}$ in the y direction, so that its circularly polarized electric vector is given (cf. eq. (7)) by $\boldsymbol{E}_\eta = E_0(\hat{\boldsymbol{z}} - i\eta\hat{\boldsymbol{x}})/\sqrt{2}$. We look for electronic polarization in the z direction given by

$$(P_e)_z = \langle J^f_z\rangle = \frac{\sum_{m_f m_i} m_f |\langle f_s|\boldsymbol{E}_\eta\cdot\boldsymbol{E}1|i_s\rangle + \langle f_{PNC}|\boldsymbol{E}_\eta\cdot\boldsymbol{E}1|i_{PNC}\rangle|^2}{\sum_{m_f m_i} |\langle f_s|\boldsymbol{E}_\eta\cdot\boldsymbol{E}1|i_s\rangle + \langle f_{PNC}|\boldsymbol{E}_\eta\cdot\boldsymbol{E}1|i_{PNC}\rangle|^2}, \tag{15}$$

where i and f denote initial and final states. Using eq. (14) in this expression, the sums over m_f and m_i give in general a nonvanishing result proportional to η. For example, the Stark amplitude for $m_f = m_i$ transitions, proportional to $i\eta E_0 E_s$, interferes with the PNC amplitude for the same transitions which is also pure-imaginary and is odd in m_f. Thus, a measurement of $\langle J^f_z\rangle$ provides the pseudoscalar $\boldsymbol{J}^f\cdot\eta\boldsymbol{k}\times\boldsymbol{E}_s$ which reveals the PNC interaction of the atom. More details of the calculation of eq. (15) are given in section 5.2.

3. Magnitude of neutral current weak interaction in atoms

Here we will start with the relativistic neutral current interaction between electrons and nucleons and use it with suitable approximations to discuss the amplitudes of parity mixing in atoms. Time-reversal symmetry is assumed throughout. The PNC neutral current interaction between electrons makes only a relatively small contribution in heavy atoms [31] and is not present in hydrogen. Therefore it will not be considered here.

In gauge theories, fermion currents interact via intermediate bosons, such as the photon in EM processes. In the weak interaction, these bosons must have very large masses (~100 GeV). In atoms it is clearly adequate to replace the propagator for such massive bosons by a contact function, and the weak interaction reduces to a current–current interaction form. The parity nonconserving part is given, in terms of the Fermi coupling constant G_F (=89.6 eV (fm)^3), the nucleon and electron wave functions ψ_N

and ψ_e, and isospin operator τ_3, by [33]

$$H_{PNC} = \frac{G_F}{\sqrt{2}}[\bar{\psi}_N\gamma_\mu(v_0 + v_1\tau_3)\psi_N\bar{\psi}_e\gamma^\mu\gamma^5\psi_e + \bar{\psi}_N\gamma_\mu\gamma^5(a_0 + a_1\tau_3)\psi_N\bar{\psi}_e\gamma^\mu\psi_e] . \tag{16}$$

This operator is to be used in eq. (1) to find the PNC dipole moments of atoms.

In the Weinberg–Salam theory, the parameters of H_{PNC} are given in terms of a single parameter θ_w:

$$\begin{aligned} v_0 &= -\sin^2\theta_w , & a_0 &= 0 \\ v_1 &= \tfrac{1}{2}(1 - 2\sin^2\theta_w) , & a_1 &= \tfrac{1}{2}(1 - 4\sin^2\theta_w)g_A \end{aligned} \tag{17}$$

where $g_A \cong 1.25$ is the axial vector coupling constant of neutron beta decay. The best current experimental value of θ_w based upon high energy lepton–nucleon scattering is given by [25, 34]:

$$\sin^2\theta_w = 0.23 \pm 0.01 . \tag{18}$$

If radiative corrections are taken into account, the value of $\sin^2\theta_w$ to be used in the atomic physics formulas given here is reduced by several percent from the value given in eq. (18) [25, 34], depending upon the relative number of neutrons and protons (down and up quarks) in the nucleus. For example, in the case of cesium, the effective value of $\sin^2\theta_w$ becomes 0.207 ± 0.001.

Frequently, one uses the vector and axial-vector coupling coefficients C_1 and C_2 for the protons and neutrons, where

$$\begin{aligned} C_{1p} &= v_0 + v_1 = \tfrac{1}{2}(1 - 4\sin^2\theta_w) \\ C_{1n} &= v_0 - v_1 = -\tfrac{1}{2} \\ C_{2p} &= a_0 + a_1 = \tfrac{1}{2}(1 - 4\sin^2\theta_w)\, g_A \\ C_{2n} &= a_0 - a_1 = -\tfrac{1}{2}(1 - 4\sin^2\theta_w)\, g_A . \end{aligned} \tag{19}$$

The second form in each case is that given by the Weinberg–Salam theory. Independently of gauge theories, we could have written eq. (16) as a phenomenological current–current interaction with parameters to be determined by experiment.

Nonrelativistically,

$$\gamma_0 \sim 1 , \qquad \boldsymbol{\gamma}\gamma^5 \sim \boldsymbol{\sigma} , \qquad \gamma^5 \sim \boldsymbol{\sigma}\cdot\boldsymbol{p}/mc . \tag{20}$$

In an atomic nucleus, the nucleons are nonrelativistic, so we may approximate eq. (16) by

$$H_{PNC} = \frac{G_F}{\sqrt{2}}\sum_{eN}\left[C_{1N}\int \psi_N^+\psi_N\psi_e^+\gamma^5\psi_e\, d\boldsymbol{r} + C_{2N}\int \psi_N^+\boldsymbol{\sigma}_N\psi_N\cdot\psi_e^+\boldsymbol{\alpha}\psi_e\, d\boldsymbol{r}\right], \tag{21}$$

where N stands for n or p, and the summation is over all electrons and nucleons in the atom. We have used $\bar{\psi} = \psi^+\gamma^0$ and $\boldsymbol{\gamma} = \gamma^0\boldsymbol{\alpha}$. The terms in C_{1N} are additive for all the nucleons because the electronic wave function has approximately the same phase over the entire nucleus. The terms in C_{2N} depend upon nuclear spin and have a net contribution only from unpaired nucleons.

In heavy atoms the C_1 terms normally dominate and provide a total interaction for each electron of the form

$$H_{\mathrm{PNC}}^{(1)} = \frac{G_{\mathrm{F}}}{\sqrt{2}} \frac{Q}{2} \int \rho_{\mathrm{N}} \psi_{\mathrm{e}}^{+} \gamma^5 \psi_{\mathrm{e}} \, \mathrm{d}\boldsymbol{r} \tag{22}$$

where $Q = 2(ZC_{1\mathrm{p}} + \eta C_{1\mathrm{n}})$. Z and η are the numbers of protons and neutrons in the nucleus, and ρ_{N} is the nuclear density. In the Weinberg–Salam theory,

$$Q = Z(1 - 4\sin^2 \theta_{\mathrm{w}}) - \eta \,. \tag{23}$$

There are some cases [24] in heavy atoms where $H_{\mathrm{PNC}}^{(2)}$, the interaction containing the $C_{2\mathrm{N}}$ terms, might still be measurable, even though it is much smaller than $H_{\mathrm{PNC}}^{(1)}$.

In principle the hydrogen experiments can be made equally sensitive to either $C_{1\mathrm{p}}$ or $C_{2\mathrm{p}}$. Experiments in both hydrogen and deuterium could be combined to yield $C_{1\mathrm{n}}$ and C_{2n} as well.

Thus far we have retained the form of H_{PNC} which is correct for arbitrary electron energy, since in heavy atoms the electrons are indeed fully relativistic near the nucleus where they contribute to H_{PNC}. However, the nonrelativistic form of H_{PNC} is useful for calculations in light atoms and also has some conceptual value in heavy atoms as well. Making the nonrelativistic approximations of eq. (20) for the Dirac operators in eq. (21) we obtain the nonrelativistic potential for a single electron interacting with a point nucleus at $r = 0$;

$$V_{\mathrm{PNC}}^{\mathrm{nr}} = \frac{G_{\mathrm{F}}}{m_{\mathrm{e}} c \sqrt{2}} \sum_{\mathrm{N}} \frac{\delta(\boldsymbol{r})}{2} [C_{1\mathrm{N}} \boldsymbol{\sigma}_{\mathrm{e}} \cdot \boldsymbol{p}_{\mathrm{e}} - C_{2\mathrm{N}} (\boldsymbol{\sigma}_{\mathrm{N}} \cdot \boldsymbol{p}_{\mathrm{e}} + \mathrm{i} \boldsymbol{\sigma}_{\mathrm{N}} \cdot \boldsymbol{\sigma}_{\mathrm{e}} \times \boldsymbol{p}_{\mathrm{e}})] + \mathrm{h.c.} \tag{24}$$

The PNC aspect of the potential is evident from the pseudoscalar combinations of the vectors in eq. (24). This interaction will mix electronic states of opposite parity. Only mixing between $s_{1/2}$ and $p_{1/2}$ states need be considered usually, because other states make a negligible contribution at the origin.

The matrix elements of $V_{\mathrm{PNC}}^{\mathrm{nr}}$ rise rapidly with atomic number Z, as first pointed out by Bouchiat and Bouchiat [15]. This behavior can be seen by using an approximate expression given by Fermi and Segré [35] for the probability density of an ns-electron at the origin:

$$|\psi_{\mathrm{s}}(0)|^2 = \frac{Z Z_0^2}{\pi (n - \sigma)^3 a_0^3} \left(1 - \frac{\mathrm{d}\sigma}{\mathrm{d}n}\right), \tag{25}$$

where $Z_0 \sim 1$ is the total charge seen by the electron, and σ is the quantum defect. (The formula was originally derived for alkali metals, but the qualitative behavior is more general.) Note the factor of Z which indicates how much the wave function is "pulled in" where the nuclear charge is incompletely shielded. The momentum operator acting on p states brings out another factor of Z,

$$\left| \frac{\hbar}{\mathrm{i}} \frac{\partial}{\partial r} \psi_{\mathrm{p}} \right|_0 \sim Z \frac{\hbar}{a_0} |\psi_{\mathrm{s}}(0)| \,. \tag{26}$$

The coherence over the nucleus for $H_{\mathrm{PNC}}^{(1)}$ contributes the factor Q of eq. (23) which rises roughly as Z. The nonrelativistic result is a Z^3 dependence of $\langle n' \mathrm{p}_{1/2} | V_{\mathrm{PNC}}^{\mathrm{nr}} | n \mathrm{s}_{1/2} \rangle$.

Using eqs. (24), (25) and (26) we arrive at the expression

$$\langle n'p_{1/2}|V_{\rm PNC}^{\rm nr}|ns_{1/2}\rangle \sim \frac{G_{\rm F}}{4\pi\sqrt{m_{\rm e}}}\frac{Z^2QhK_{\rm r}}{ca_0^4(n'-\sigma')^{3/2}(n-\sigma)^{3/2}}$$
$$\sim 10^{-16}Z^2QK_{\rm r}, \tag{27}$$

where $K_{\rm r}$ is a relativistic correction factor which increases with Z, becoming $\cong 3$ for Cs and $\cong 10$ for Bi. Equation (27) was first derived by Bouchiat and Bouchiat [15] and is useful for estimating the order of magnitude of PNC effects in atoms. For example, using eqs. (1) and (27) we find that $\mathscr{E}_{\rm PNC} \cong 10^{-9}\, ea_0$ for heavy atoms such as Tl, Bi or Pb. In a normal M1 transition, $\mathscr{M} \lesssim 10^{-2}\, ea_0$. Thus the measurable quantity R (see eq. (12)) in optical rotation experiments will be $R \cong 10^{-7}$ which is roughly the size of the PNC rotation angles observed. Of course, complete relativistic calculations of $\mathscr{E}_{\rm PNC}$ are required for accurate comparison with experiments.

4. Optical rotation experiments

4.1. General experimental features

Experiments designed to look for optical rotation in heavy metal vapors began in 1974 in Seattle [16], Oxford [7] and Novosibirsk [17, 36]. A fourth experiment began more recently in Moscow [37]. All four groups chose initially to look for optical activity in atomic bismuth because bismuth has allowed M1 absorption lines which are accessible with tunable lasers available at the time the experiments were begun. The Seattle group is now also measuring optical rotations in lead and thallium, using lasers which have only recently become available.

For illustration, we show the bismuth energy levels and the transitions studied by the different groups in fig. 1. The Seattle experiment uses the $^4S_{3/2} \rightarrow {}^2D_{3/2}$ line at 876 nm. All of the other groups use the $^4S_{3/2} \rightarrow {}^2D_{5/2}$ line at 648 nm, although the Oxford group has begun a second experiment at the 876 nm line as well. The PNC admixed electric dipole moments for the 876 nm transition are indicated by E1 and E1′.

Comparisons between theoretical predictions and experimental results are usually made in terms of the quantity $R = \mathrm{Im}(\mathscr{E}_{\rm PNC}/\mathscr{M})$, which is related to the rotation $\phi_{\rm PNC}$ in eq. (12). In that equation we see that the rotation $\phi_{\rm PNC}$ follows a dispersion curve $(n-1)$, with the maximum change in $\phi_{\rm PNC}$ occurring across the absorption line center from one dispersion peak to the other, with magnitude

$$\Delta\phi_{\rm PNC} \sim l\kappa_0 R, \tag{28}$$

where an isolated Lorentz-shaped line is assumed. This expression serves as a useful estimate even when the line shape is not Lorentzian. Predicted magnitudes of $\Delta\phi_{\rm PNC}$ are of order 10^{-7} rad. per absorption length $l\kappa_0$. The efforts of all experimenters are devoted to assessing the value of this asymmetric rotation associated with PNC, while discriminating against other rotations which are not related to PNC.

In general, the transitions show hyperfine structure. For illustration, fig. 2 gives theoretical PNC and transmission curves for the 876 nm line of atomic bismuth, together with the Faraday rotation profile

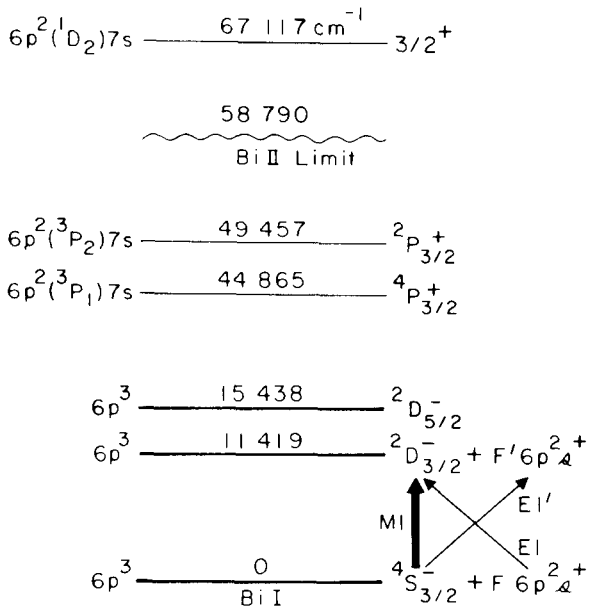

Fig. 1. Atomic bismuth energy levels. Although the levels are given the traditional *LS* designation, *LS* coupling is completely broken in a heavy atom such as Bi.

discussed in the next section. The hyperfine structure of the 876 nm line consists of nine prominent M1 lines and several smaller electric quadrupole transitions with an intensity about 10^{-2} that of the M1. All of these M1 lines have been studied for PNC rotation. The bismuth hyperfine structure at 648 nm is composed of 12 mixed M1 and E2, and 6 pure E2. The E2 intensity is about 0.2 that of the M1. The

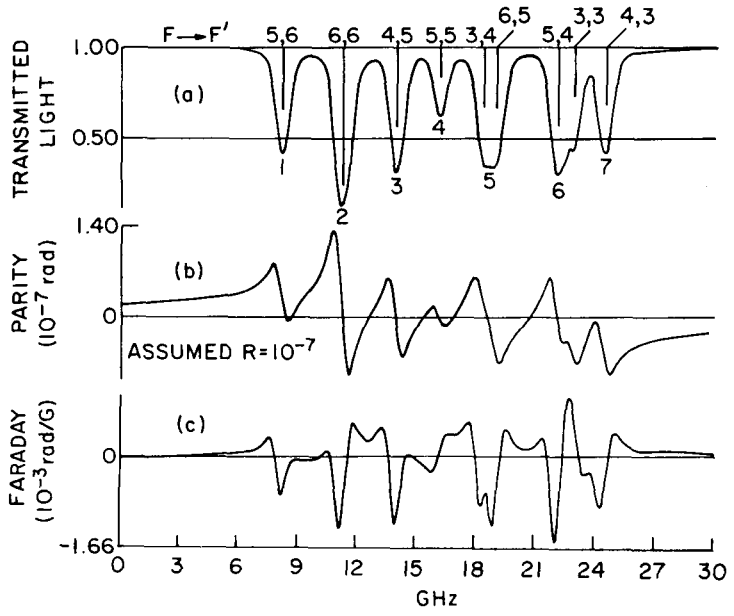

Fig. 2. Theoretical Faraday and parity rotation curves and transmission curve for the 876 nm transition in atomic bismuth.

strength of the 648 nm line is about one-sixth that of the 876 nm line, which has resulted in the use of higher bismuth densities in those experiments at 648 nm.

Background absorption can also be important. For example, the observed absorption at 876 nm reproduces the theoretical M1 features of fig. 2, whereas the 648 nm absorption pattern is dominated by resonance lines of bismuth molecular dimers. Fortunately, the Faraday rotation of the molecules is much smaller than that of the atoms because the molecular states producing this band have zero electronic angular momentum. While this permits one to unambiguously identify the atomic lines by their Faraday rotation, the molecular absorption limits the usable optical depth to about one absorption length on the strongest M1 component. On the other hand, the molecular background offers test lines for checking systematic effects.

4.1.1. Faraday rotation

An optical rotation which offers systematic hazards, but which serves as a valuable calibration tool as well, is the Faraday rotation [38]. Faraday rotation of plane polarized light occurs in a medium when a magnetic field is present. The rotation is proportional to the component of the magnetic field along the direction of light propagation. As such, the sign of the rotation (as defined below eq. (12)) reverses when either the magnetic field is reversed, or the direction of propagation of the light reverses. Note that this behavior under reversal of the light direction is the opposite of PNC rotation.

The contribution to the Faraday effect from each hyperfine component of the transition is conveniently divided into two parts. One is symmetric about the line center of the hyperfine component, and the other is antisymmetric. The symmetric portion arises because the magnetic field causes a Zeeman splitting of each hyperfine component. Because of the Zeeman splitting and the selection rules governing circularly polarized light, the index of refraction curve associated with right circularly polarized light is shifted in frequency with respect to the index of refraction curve associated with left circularly polarized light. Thus, for the ith hfs component, the two circular components of plane polarized light have a difference in index of refraction $n_+ - n_-$, which from the first of eqs. (12), leads to a symmetric Faraday rotation,

$$\phi^i_{\mathrm{Fs}}(\nu) \cong \frac{\mu_i B l}{h\lambda} \frac{\mathrm{d}n_i}{\mathrm{d}\nu}, \tag{29}$$

where μ_i is of the order of a Bohr magnetron, and $\nu = c/\lambda$. At the center ν_0 of an absorption line having frequency width ν_w, this rotation becomes

$$\phi^i_{\mathrm{Fs}}(\nu_0) \cong \frac{\mu_i B}{h\nu_w} (l\kappa_{0i}). \tag{30}$$

From this approximation, we see that magnetic field strengths of 10^{-4} gauss can produce symmetric rotations comparable to the expected size of $\Delta\phi_{\mathrm{PNC}}$, for typical Doppler-broadened lines of width $\nu_w \cong 1$ GHz.

The antisymmetric portion of the Faraday effect arises from the fact that the magnetic field mixes pairs of hyperfine states of a given J proportionally to m_F, the magnetic quantum number of the pair. The state mixing results in a different transition amplitude for different Δm_F values. This causes the refractive index curve to differ in size (but not center frequency) for the two circular polarizations. As in

eq. (29) we find the (in this case antisymmetric) rotation

$$\phi^i_{\mathrm{Fa}}(\nu) \cong \frac{\mu_i B l}{h\lambda} \frac{n_i - 1}{\Delta\nu_i}, \tag{31}$$

where $\Delta\nu_i$ is of the order of the splitting among the hyperfine energy levels. The change between the dispersion peaks on each side of the line-center is

$$\Delta\phi^i_{\mathrm{Fa}} \cong \frac{\mu_i B}{\Delta\nu_i}(l\kappa_{0i}). \tag{32}$$

This rotation also becomes significantly large compared to $\Delta\phi_{\mathrm{PNC}}$ for field strengths of $\sim 10^{-4}$ gauss for typical hyperfine splitting $\Delta\nu \cong 1$ GHz. The total Faraday rotation is

$$\phi_{\mathrm{F}} = \sum_i [\phi^i_{\mathrm{Fs}} + \phi^i_{\mathrm{Fa}}]. \tag{33}$$

While the antisymmetric Faraday rotation is easy to confuse with the PNC rotation, it can be eliminated in the experiments if the magnetic field is adjusted to make the symmetric Faraday rotation vanish.

In a practical case, the precise formulas for the effects (29) and (31) can be complicated, and the calculations, although straightforward, are very tedious [38]. Figure 2 shows the total Faraday rotation pattern calculated for the 876 nm line in atomic bismuth.

4.1.2. Measurement of small rotations

The small rotations involved in these experiments can be measured by placing a column of the desired metal vapor between two crossed polarizers. A slight rotation of the plane of polarization of light in the vapor between the two polarizers will produce a large fractional change in the light intensity I_s transmitted by the second polarizer. If ϕ is the angle by which the plane of polarization differs from the plane of minimum transmission through the second polarizer, then I_s varies as $\sin^2\phi$, and for $\phi \ll 1$,

$$I_s = I_0(\phi_0^2 + \phi^2), \tag{34}$$

where I_0 is the incident light intensity and ϕ_0 is a constant (called the "extinction angle") dependent upon the polarizer and light beam quality. In practice, $\phi = \phi_M + \delta\phi$, where $\delta\phi$ is a small rotation angle, such as that due to the PNC rotation, and ϕ_M is an offset angle which may be modulated between two or more values. The rotation $\delta\phi$ produces its largest fractional intensity change $\delta I/I$ when ϕ_M equals ϕ_0, in which case $\delta I/I = \delta\phi/\phi_0$. If ϕ_0^2 equals 10^{-7}, a typical value of extinction for good calcite polarizers, then a rotation of $\delta\phi = 3 \times 10^{-7}$ radian will produce $\delta I/I \sim 10^{-3}$. It is this enhancement in the fractional effect which makes the rotation experiments feasible.

4.1.3. Angle resolution

Shot noise in the rotation experiments is very small. The rms fluctuation in angle due to shot noise in the detected photons is

$$\Delta\phi_{\mathrm{shot}} \sim [h\nu\Gamma/\varepsilon I_0]^{1/2}, \tag{35}$$

where Γ is the observation bandwidth, $h\nu$ is the photon energy, and ε is the detector quantum efficiency.

The lasers used in these experiments typically produce powers greater than 2 mW. The detectors often are of nearly unit quantum efficiency. Thus, in one second, $\Delta\phi_{\text{shot}} < 10^{-8}$ radian. Even with the decreased efficiency of photomultiplier tubes, and less light intensity in experiments which use many absorption lengths of bismuth vapor, $\Delta\phi_{\text{shot}} < 10^{-7}$ radian in one second. In practice, the noise in the measured angles often turns out to be larger than the shot noise limit, due to a combination of mechanical and optical instabilities, and detector noise in some cases. In the most recent experiments, 10^{-8} radian at a point can usually be resolved in less than 1 minute of averaging time. The major problems, as discussed later, come from unwanted changes in rotation angle with wavelength.

4.2. Atomic calculations of PNC optical rotation

4.2.1. Central field independent particle model

The starting point for most calculations has been to approximate the exact electronic wave function by a single determinant of independent particle wave functions (IPM) derived from a central potential. In this approximation, the E1 matrix element introduced in eq. (1) may be written as

$$\mathscr{E}_{\text{PNC}}(kj) = \sum_l \left\{ \frac{(k|H_{\text{PNC}}|l)\,(l|\boldsymbol{E}1|j)}{\varepsilon_k - \varepsilon_l} + \frac{(k|\boldsymbol{E}1|l)\,(l|H_{\text{PNC}}|j)}{\varepsilon_j - \varepsilon_l} \right\}, \tag{36}$$

where the single-particle operators H_{PNC} and $\boldsymbol{E}1$ permit the many-electron determinants and energies to be replaced by single (valence) electron states and energies denoted here by $|n)$ and ε_n. The sum over intermediate states in eq. (36) includes both unoccupied and occupied states. The former correspond to holes in the core electronic configuration due to excitation of a core electron into the open (valence) shell.

4.2.2. Intermediate coupling

Bismuth provides a good example of the coupling procedure used in heavy atoms. The five lowest lying states of bismuth, shown in fig. 1, all have the central field configuration $6p^3$. It is necessary to take linear combinations of (Slater) determinants in order to construct wave functions of good J and M within this configuration. The two extreme cases are L–S and j–j coupling. Because relativistic effects are important in heavy atoms, it is convenient to use a j–j representation in bismuth. The actual states, which are intermediate between L–S and j–j coupling, are then a linear combination of j–j coupled states. The intermediate coupling coefficients can be determined from an analysis of hyperfine splitting. The calculations of PNC effects are not very sensitive to the uncertainties in these coefficients.

4.2.3. Calculation of $M1$

As is evident from eq. (6), the calculation of M depends only on the intermediate coupling coefficients, and not on details of the radial wave function. Thus the M1 matrix element is known more reliably than the E1 matrix element.

4.2.4. Central field and other lowest-order results

Calculations at the level of accuracy discussed thus far have been carried out using various self-consistent potentials or parametric potentials. These potentials take into account, in varying

Table 1
Theoretical values of PNC quantities in bismuth and lead. $Q \equiv Z(1-4\sin^2\theta_w)-\eta$

Transition (nm)	$R = \mathrm{Im}(\mathscr{E}_{PNC}/\mathscr{M})$	Method
Bi (876)	$-1.2\times10^{-9}Q$	Central field only (average of a, b, c, d)
	$-1.1\times10^{-9}Q$	Semi-empirical (d)
	$-0.95\times10^{-9}Q$	First-order perturbations plus shielding (e)
	$-0.66\times10^{-9}Q$	Relative Hartree–Fock (with shielding) (f)
Bi (648)	$-1.5\times10^{-9}Q$	Central field only (average of b, c, d)
	$-1.3\times10^{-9}Q$	Semi-empirical (d)
	$-1.1\times10^{-9}Q$	First-order perturbations plus shielding (e)
	$-0.88\times10^{-9}Q$	Relativistic Hartree–Fock (with shielding) (f)
Pb (1279)	$-1.04\times10^{-9}Q$	Semi-empirical (d)
	$-1.56\times10^{-9}Q$	Relativistic Hartree–Fock (without shielding) (g)

(a) Ref. [33] (Henley and Wilets).
(b) Ref. [33] (Brimicombe et al.).
(c) Ref. [39].
(d) Ref. [46].
(e) Ref. [44].
(f) Ref. [43].
(g) Ref. [47].

degrees, some of the exchange effects of a Hartree–Fock IPM treatment. The results of the different central field calculations in bismuth agree with each other; the average value for each transition is shown in table 1. However, as discussed in the next section, there are large corrections that must be applied to all these values. In particular, the noncentral forces due to the electron–electron interactions couple configurations of different nl, and can have a decisive effect.

An interesting point has been emphasized by Carter and Kelly who carried out a central field calculation using both the "length" $e\boldsymbol{r}\cdot\boldsymbol{E}$ and "velocity" $2e\boldsymbol{p}\cdot\boldsymbol{A}/mc$ forms of the $E1$ operator [39]. The two forms should give the same answer in an exact calculation, but can differ in approximate treatments. Carter and Kelly found the same central field result as others with the length form, but a substantially different result with the velocity form. The significance of this disparity is not completely clear, although a number of authors have concluded that the length form is more trustworthy [40, 41].

4.2.5. Noncentral configuration mixing – Bismuth

There have been a number of calculations that go beyond the central field approximation in bismuth. In particular, an elegant formalism for attacking the problem was devised by Sandars [42], in which H_{PNC} is incorporated into the HF solution *before* expanding in the residual electron–electron interaction. The most complete calculations of PNC to date are by Sandars and his colleagues [40] at Oxford, and by Märtensson, Henley and Wilets [43] at Seattle.

The Oxford group began by calculating all corrections to first order in the residual electron–electron interaction energy. Their treatment included both the effect of mixing of different nl configurations and corrections due to the difference between their parametric potential and true Hartree–Fock. They found moderately small corrections except for a class of terms which are due to dipole shielding. Physically, the shielding comes from core electrons that are polarized by the electric vector in the radiation field and cancel some of the effect of this field on the transition electron. The shielding in bismuth is caused mainly by the highly polarizable 6s and 6p electrons shielding one another. Harris, Loving and Sandars [44] approximated the shielding effect to all orders of a self-consistent Hartree treatment. Their result showed approximately a 50% reduction of PNC in the bismuth transitions of interest. A similar

calculation of the shielding of PNC in bismuth using a different effective potential was carried out later by Fortson and Katz [45], who found an effect of comparable size.

Sandars et al. have now produced a calculation for bismuth [40] which includes shielding to all orders, and the remaining noncentral effects to first order. Table 1 includes their results.

In Seattle, Märtensson et al. [43] took as a starting point a thorough Hartree–Fock treatment. They introduced the noncentral electron–electron interactions as first-order perturbations except that, as above, the core shielding was carried out self-consistently to all orders. The shielding of the PNC potential as well as of the external optical electric field was included. Their lowest order HF result is smaller in magnitude than other lowest order IPM values (the central field entries in table 1), but the further reduction by shielding turns out to be less than that in the Oxford treatment. The net result of Märtensson et al. is somewhat smaller (30%) than Oxford's, as shown in table 1.

A semi-empirical approach to making corrections to the central field model was taken by Novikov, Sushkov and Khriplovich before shielding corrections were considered [46]. They calculated E1 matrix elements in Au, Hg and Tl using a parametric potential. They found that the calculated 6p–*n*s matrix elements agreed well with experiment, with the exception that the 6p–6s element was too large by a factor of 1.6 in Tl. Although the optical $6s \rightarrow 6p$ transition is not observed in bismuth, it is the dominant (56%) matrix element in the sum, eq. (1). On this basis, they reduced this calculated PNC-induced E1 matrix element in Bi by a factor 1/1.6. Because the 6p and 6s wave functions overlap mainly within the atomic core, shielding should affect the 6p–6s matrix element strongly. It should not affect the 6p–7s matrix element so strongly, which agrees with the findings of Novikov et al. in Tl. Thus, the semi-empirical approach probably accounts for some shielding and perhaps other, higher-order effects. However, it is not obvious just how accurate the approach is. Bi is more polarizable than Tl due to two extra valence electrons. Novikov et al. end up with slightly larger magnitudes for R than Sandars et al. and Märtensson et al. in bismuth, as shown in table 1.

We select as the best theoretical value in bismuth the average of these three calculations, each of which goes beyond the central field IPM approximation. Thus we take, with $\sin^2\theta_w = 0.23$,

$$R_{\text{theory}}(\text{Bi } 876) = (-11 \pm 3) \times 10^{-8}$$
$$R_{\text{theory}}(\text{Bi } 648) = (-13 \pm 4) \times 10^{-8}, \tag{37}$$

where the indicated uncertainties accommodate the disparity among the results of these three quite different approaches to the problem.

4.2.6. Lead calculations

The other atom for which we have experimental optical rotation results is lead. Two values that go beyond the central field approximation are shown in table 1, the first obtained by Novikov et al. [46] using their semi-empirical approach, and the second a preliminary result from a complete time dependent HF calculation undertaken by Sandars and Märtensson [47]. We take the average of these latter two numbers as the current best value for the 1.28 μm transition in lead, with $\sin^2\theta_w = 0.23$,

$$R_{\text{theory}}(\text{Pb } 1.280) = -(13 \pm 2) \times 10^{-8}. \tag{38}$$

4.3. Measurements on the 876 nm line of bismuth

4.3.1. Experimental layout of the Seattle experiment

The principal experimental features of all of the optical rotation experiments are the same, with some major variations in implementation. We will illustrate these features in detail with the Seattle bismuth experiment, and then describe somewhat briefly the other optical rotation experiments.

Figure 3 illustrates the Seattle experimental layout. The output from a single-mode laser diode is passed through a bismuth cell which is placed between two crossed calcite prism polarizers. Both Nicol and Glan–Thompson prisms have been used at different times for these measurements. A typical extinction value for these polarizers is about 10^{-7}. A water-filled glass cell held within a solenoid acts as an angle modulator, utilizing the Faraday effect in that substance. A sinusoidal modulation with amplitude $\phi_m \cong 10^{-3}$ radian and frequency of 1 kHz is used. As can be seen from eq. (34), a 1 kHz term appears in the signal after the second polarizer that is proportional to $2\phi_m \delta\phi$, where $\delta\phi$ is the angle of rotation between the polarizers. Therefore detection of the fundamental modulation frequency after the analyzer gives the rotation signal. A second winding on the water cell is used to correct the average angle offset, as measured over a period of about one minute. This control holds the polarizers to extinction within 10^{-6} radian without interfering with the wavelength dependent rotation signal of interest, which occurs with a characteristic time of less than 0.1 second as the laser wavelength is swept. This control combined with using a reference detector to normalize the intensity makes the rotation signal highly insensitive to changes in light intensity at the analyzer, and in particular rejects the bismuth absorption pattern. A change in I_0 of 50% affects the angle measurement by 10^{-8} radian.

Bismuth metal is contained in a meter long, 2.5 cm diameter alumina tube which is placed within a four inch diameter tube with water-cooled quartz windows. These and the Faraday modulator windows are wedged and AR coated to avoid interference effects with reflected light. The smaller diameter tube can be moved easily in and out of the optical path without moving the windows, thereby quickly changing the bismuth absorption. Clamshell heaters which surround the bismuth cell are used to regulate the temperature between 1250 K and 1400 K, producing up to ten absorption lengths on the

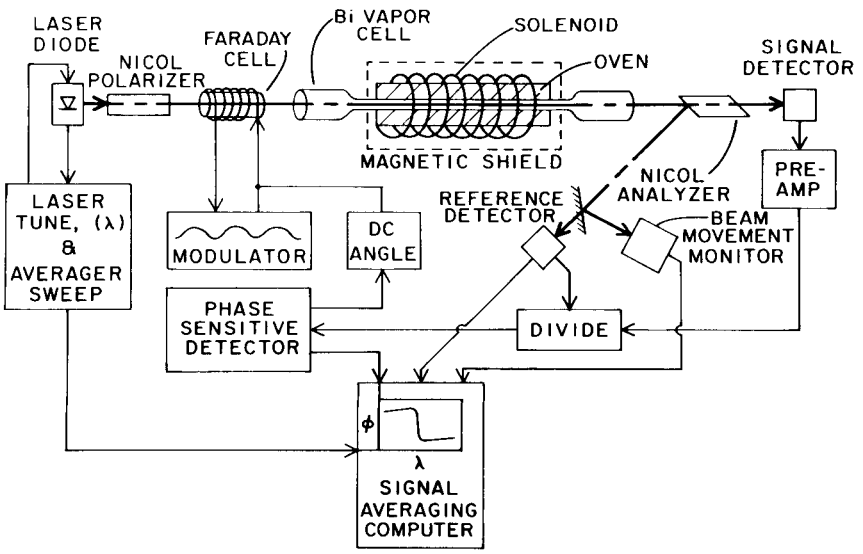

Fig. 3. Block diagram of the Seattle optical rotation experiment.

strongest hyperfine component at 876 nm. A buffer gas of helium at about 4000 Pa (30 torr) prevents bismuth from migrating to the cold windows. Two layers of permalloy magnetic shielding are used to remove external magnetic fields. A coil wrapped about the bismuth cell serves to reduce any residual longitudinal field still further, and also to produce a known magnetic field for calibration using the bismuth Faraday effect.

PIN diode detectors having 80% quantum efficiency at 876 nm are used both to gather the rotation signal and to guard against certain systematics. In addition to the detector which collects the 1 kHz angle modulation signal after the analyzer prism, a reference detector monitors the reflected light from the front face of the prism for use in normalizing the rotation signal amplitude. A four quadrant PIN diode uses light from a beamsplitter to evaluate position movement of the laser beam. Still other detectors before the first polarizer provide a reference for formation of normalized absorption curves, and continuous evaluation of the laser mode structure.

4.3.2. Diode lasers

Several different types of gallium–aluminum–arsenide diode lasers have been used by the Seattle group, with the useful PNC data coming from lasers of two different structures, three transverse junction stripe (TJS) diode lasers [48], and one channeled-substrate-planar (CSP) laser [49].

Diode lasers offer the advantages of small size, low cost, great stability, and simplicity of operation. The active region of the TJS laser is about 0.5 μm by 2 μm, and that of the CSP laser is about 2 μm by 10 μm. These small emitting areas result in rapidly diverging light which must be collimated with suitable optics. It is also sometimes necessary to use a type of directional coupler to prevent reflected light from affecting the mode properties of the laser.

The linewidth of the TJS laser is about 150 MHz, as measured with a Fabry–Perot interferometer, while that of the CSP laser is less than 50 MHz as deduced from the line shapes of the bismuth hyperfine structure. Both lasers have additional longitudinal modes, but they are spaced about 0.4 nm apart, while the entire bismuth hfs extends over only 0.05 nm. In addition, approximately 95% of the total output light lies on the desired laser mode. The TJS laser did sometimes exhibit small side modes spaced 1–2 GHz to each side of the main mode. It is believed that these modes have not seriously affected the results obtained, but the additional measurements using the CSP type lasers are a good check on this possible systematic.

The lasers tune about 0.01 nm/mA of injection current above threshold, and about 0.2 nm/°C in temperature. These tuning rates dictate current regulation of about 10^{-6} A, and temperature regulation on the order of 10^{-4} °C. Under these conditions the amplitude of the laser output is highly stable, requiring no further intensity stabilization.

The TJS lasers used in these experiments emit a maximum of 3 mW from each of their two facets, and the CSP laser produces up to 15 mW per facet.

4.3.3. Data acquisition

When accumulating data a triangularly shaped modulation is applied to the laser diode injection current in order to sweep the laser wavelength back and forth over the Bi 876 nm line. A portion of the hfs of this line is selected, and the wavelength of the laser adjusted to match that range by setting the average current, temperature, and modulation amplitude to appropriate values. As mentioned earlier, the water-filled Faraday cell modulates the rotation angle at a 1 kHz rate.

The rotation signal is divided by the amplitude of the reference signal in an analog divider. This normalized signal is demodulated by a phase sensitive detector (PSD) at 1 kHz. The resulting rotation

signal is then stored on one channel of the minicomputer. The rotation correction signal which keeps the polarizers centered at extinction is also derived from the PSD output. A second channel of the minicomputer accepts the reference signal, which serves as a record of the absorption pattern. Still more computer memory is devoted to monitors of beam position and mode properties.

Figure 4 shows experimental points of both Faraday rotation and transmission taken in the Seattle experiment. These data demonstrate excellent agreement with the theoretical curves.

PNC data are taken on odd numbered cycles of the triangular wavelength sweep during which the bismuth Faraday coil is adjusted to give nearly zero residual Faraday effect. On these cycles the oven heaters are switched entirely off, thereby avoiding an observed spurious effect due to AC Faraday rotation which can mimic the PNC rotation curve if the laser wavelength sweep has any synchronous AC modulations.

On even numbered cycles the oven heaters are switched into a regulating mode. At the same time a large current is passed to the bismuth Faraday coil in order to produce a calibration curve. A slightly different current is given to the bismuth Faraday coil during the "up" sweep in wavelength than during the "down" sweep. Later, computer analysis permits the recovery of the minute difference in Faraday rotation between up and down sweeps. This difference serves as evidence of the ability to accurately measure angle changes smaller than the predicted PNC rotations.

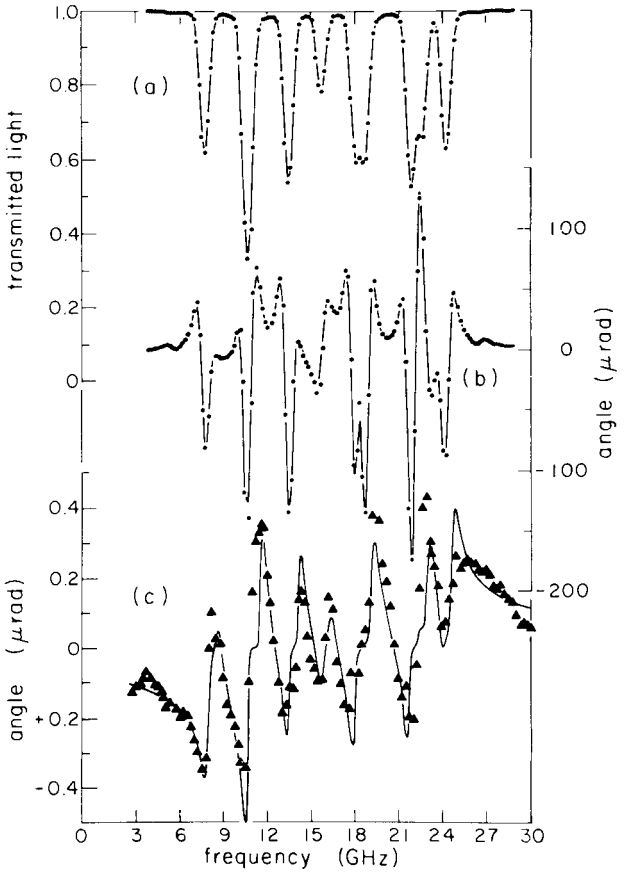

Fig. 4. Seattle experimental data for 876 nm in bismuth. (a) Transmission. (b) Faraday rotation. (c) Parity rotation. Solid curves are best fits of theoretical curves.

A sum of 1000 sweeps constitutes a data set. All data accumulated in a data set is stored on tape, for subsequent analysis. The PNC data in each set is fit to a sum of a theoretical PNC curve plus a Faraday rotation curve plus a transmission pattern. The size of the PNC fit, taken together with the measured fit to the Faraday rotation during calibration cycles, yields the value of R independently of the optical depth and of the rotation angle sensitivity. An independent calibration for R uses the measured absorption and the rotation angle sensitivity.

An analysis that makes use of all information collected with each data set seeks to find any correlations between the measured values of the PNC parameters R and other variables, such as residual ϕ_F, beam movement signal, polarizer configuration, etc. This procedure is used to set limits on known sources of systematic error, and initially helped to uncover some errors and eliminate them.

For example, one significant correlation that emerged from the early analysis occurred between the measured R and the background slope of rotation angle versus wavelength in the PNC data taken with the TJS lasers. The linewidth of these diodes, coupled with the Doppler width of the absorption lines, leads to an antisymmetric rotation about each absorption feature due to a shift of the average wavelength of the laser light actually transmitted on each side of the absorption. The observed correlation agreed well with the predicted correlation based on this model for the systematic.

For the TJS data, then, results may be obtained for data sets which average to zero background slope (and possess equal absorption lengths), or by using the observed correlation to extrapolate to zero slope on individual runs. In the more recent CSP laser results the laser linewidth is small enough that this systematic is not serious.

Of interest has been the beam movement signal, which was fitted with a PNC shaped curve. If beam movement results from refraction effects in the bismuth vapor, rotations might appear which follow a dispersive curve identical to the PNC curve. Since this systematic check was installed, no correlations have been found between the beam movement fit and the fit to PNC for the regular rotation curves.

An annoying problem has been an oscillatory dependence of the polarization angle with wavelength, apparently an interference phenomenon generated within the polarizers. In principle this background can be measured and subtracted. In practice, the pattern is too sensitive to small changes in the apparatus to permit reliable subtraction. Fortunately, the background pattern averages out over many data sets, as has been verified by tests without bismuth absorption present.

4.3.4. Results of the Seattle experiment

A list of all bismuth PNC measurements carried out in Seattle is given in table 2 [50–53]. The table

Table 2
Seattle measurements of $R = \mathrm{Im}(\mathscr{E}_{PNC}/\mathscr{M})$ in bismuth (876 nm)

Data set	Ref.	Laser	$10^8 R$
A	[50]	OPO	(-8 ± 3)
B	[51]	OPO	(-0.7 ± 3.2)
C	[52]	TJS-1	(-2.4 ± 1.4)
I	[52]	TJS-2	-10.2 ± 3.1
II	[52]	TJS-3	-11.8 ± 3.9
III	[52]	TJS-3	-9.8 ± 2.4
IV	[53]	CSP-1	-9.7 ± 2.5
V	[53]	CSP-1	-10.8 ± 1.9
Weighted average (entries I–V only)			-10.4 ± 1.7

includes the first three measurements, made without the systematic checks and controls developed later. These measurements are not included in computing the final result because they lack the quality of experimental control used in subsequent measurements. The remaining five measurements, each containing between 50 and 100 data sets and each taken under a broad range of conditions, are seen to have a common value of R to within the quoted uncertainties. These five measurements yield the resultant experimental value:

$$R_{\mathrm{exp}}(\mathrm{Bi}\,876) = (-10.4 \pm 1.7) \times 10^{-8}\,, \tag{39}$$

where the quoted error is dominantly systematic.

Figure 4c shows a sum of PNC data from 20 data sets (about 6 hours of running time) from the Spring 1980 group (data set IV) in table 2. Also shown is the ϕ_{PNC} theory curve scaled to fit the data. The evident asymmetry about each hfs component occurs in all data collected since the systematic controls have been in place.

The Seattle result in eq. (39) is in good agreement with the theoretical prediction in eq. (37), which is based on all atomic calculations that go beyond the central field model.

4.3.5. The Oxford 876 nm bismuth experiment

The Oxford group began its measurements of PNC optical rotation with the 648 nm bismuth line. That experiment will be described in the following section. The same group has undertaken more recently a completely different experiment at 876 nm [54]. This latter experiment has many features in common with the Seattle experiment already described, but differs substantially in two important respects – the laser, and the method of sweeping across the hfs pattern.

The Oxford laser at 876 nm is a dye laser with the tuned output wavelength measured and controlled by a very stable external cavity. About 100 mW of output power is available at 876 nm, with less than 1 MHz linewidth. All the power is concentrated in a single mode of the laser cavity.

The laser may be continuously tuned over a substantial portion of the Bi hfs structure at 876 nm shown in fig. 2. Because this sweep rate is relatively slow for this dye laser, a sinusoidal modulation is also applied to the cavity tuning, moving the laser wavelength quickly back and forth over a region $\Delta\lambda \cong$ one Doppler width. The center of $\Delta\lambda$ is swept slowly across the hfs spectrum. The resulting patterns of absorption, Faraday rotation, and PNC rotation resemble the derivatives of the usual curves (fig. 2).

Data collected by scanning repetitively over several adjacent hfs components is recorded on tape and then analyzed in a computer. This data is fitted to a theoretical curve $\alpha P + \beta F + \gamma B$, where P is the theoretical PNC lineshape, F is the Faraday rotation lineshape, and B is a baseline. The multiplying factors α, β and γ are determined by the fitting program.

Thus far, the Oxford group has obtained data with a statistical accuracy better than $\pm 2 \times 10^{-8}$ [47]. A published result should appear shortly.

4.4. Measurements on the 648 nm line of bismuth

In this section we describe the three experiments measuring PNC on the bismuth line at 648 nm. Unfortunately, the most recent results from each group strongly disagree with each other. It is hoped that improved measurements as discussed below will resolve this issue shortly.

4.4.1. The Oxford experiment

The Oxford group has carried out a long and careful measurement of PNC rotation on the 648 nm bismuth line. They have concentrated much of their attention on the largest hyperfine ($F = 6 \rightarrow F = 7$) component of this line. In fig. 5 is shown not only the expected PNC rotation pattern for this component, but also a comparison between the theoretical and experimental Faraday rotation curves. The agreement between these curves is very good, and verifies the interference pattern on the low frequency wing due to the pure E2 transition $F = 5 \rightarrow F = 7$ [38].

The Faraday curve exhibits two points of zero Faraday rotation between which the PNC rotation has nearly its maximum change of $\Delta\phi_{\mathrm{PNC}} \sim R$. The intent of the Oxford experiment has been to determine $\Delta\phi_{\mathrm{PNC}}$ by measuring the change in angle as the laser wavelength is switched between these two points, thereby avoiding systematic effects associated with residual Faraday rotation.

The light source used by the Oxford group is a dye laser pumped by an argon ion laser, producing several milliwatts of tunable single-mode radiation at 648 nm with a frequency stability of a few MHz. The laser cavity has longitudinal modes spaced about 400 MHz apart. The laser is made to operate on a single one of these modes by using etalons inside the cavity. Fine tuning of the laser wavelength is accomplished by changing the length of the cavity while maintaining etalon adjustment for optimum power. Frequency modulation of the laser between points of zero Faraday rotation is achieved by shifting the intra-cavity etalon tuning so as to hop 2 cavity modes (~800 MHz). The cavity mode spacing and the separation between the two points on the bismuth line can be made the same, for example, by a small adjustment of the helium buffer gas pressure and hence the pressure broadening of the bismuth line. This simple method of switching the laser wavelength causes the least disturbance of the geometry of the laser beam and the smallest systematic effect on the rotation signal.

While the basic approach has remained unchanged in the Oxford experiment, the execution of the measurement has undergone a number of refinements. The earliest results [55] which were obtained without the benefit of the computer control and systematic studies discussed below disagree with all subsequent measurements and are no longer considered to be reliable. The overall optical layout is similar to the Seattle experiment already discussed. The bismuth vapor cell and a water-filled Faraday

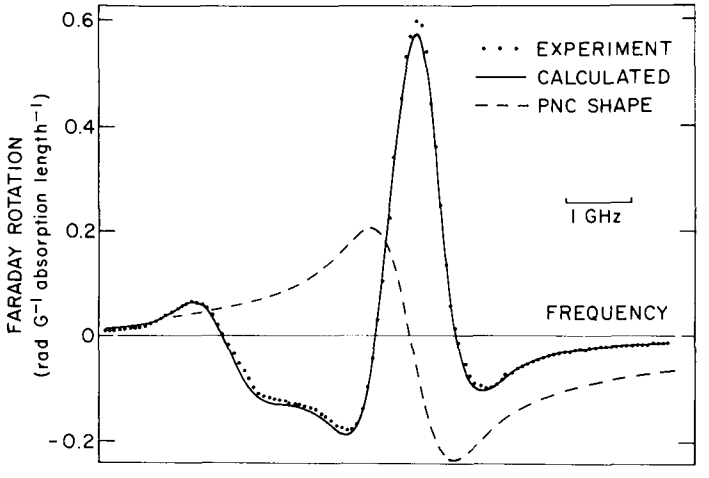

Fig. 5. $F = 6 \rightarrow F = 7$ Faraday rotation in atomic bismuth (648 nm). The points are experimental data by the Oxford group. The accompanying parity rotation curve is theoretical.

cell for angle modulation are placed between crossed calcite polarizers. The laser beam passes through these components and is detected by a silicon diode. In earlier versions, a reference beam reflected in front of the second polarizer was used to normalize the intensity of the transmitted, rotation-dependent beam. In the present version, the reference beam is unnecessary, as will be described below.

Many of the Oxford measurements have utilized a movable double-oven arrangement which allows rotations to be measured with and without a column of Bi vapor between the polarizers, but without disturbing any optical components. The change in $\Delta\phi$ between bismuth "in" and bismuth "out" constitutes the signal. Alternatively, data has been taken by changing the bismuth oven temperature rather than by moving the oven as a means of changing the Bi optical depth.

A minicomputer was programmed to control parameters and process data in all but the original measurements. In the present version the computer obtains a value for $\Delta\phi_{\mathrm{PNC}}$ by controlling the Faraday angle modulator in the following manner. The polarization angle is modulated by $\pm 2A$, through the sequence $+2A$, 0, 0, $-2A$; and then the sequence is repeated. This gives relative transmitted light intensities of $I_1 = I_0(2A + \phi_{\mathrm{PNC}})^2$; $I_2 = I_3 = I_0\phi_{\mathrm{PNC}}^2$; and $I_4 = I_0(2A - \phi_{\mathrm{PNC}})^2$, where I_0 is the incident light intensity. Division is performed digitally by the computer to give

$$\frac{I_1 - I_4}{I_1 + I_4 - I_2 - I_3} = \frac{\phi_{\mathrm{PNC}}}{2A}. \tag{40}$$

This technique avoids the limitations of analog division methods, and removes the need for an independent reference beam in order to remove the bismuth absorption pattern from the rotation signal.

The wavelength is modulated at a 1.6 Hz rate between the two sides of the absorption line. The bismuth Faraday rotation is switched on and off on each side of the line to lock the laser wavelength to the null Faraday point. PNC data is accumulated only when the Faraday rotation is off. In addition, the computer controls the number of absorption lengths by cycling the temperature of the bismuth oven.

Early measurements using the on-line computer revealed a systematic effect associated with the orientation of the second polarizer. Using a Glan–Thompson polarizer, and tilting the normal to its front face by $7\frac{1}{2}°$ from the light-beam axis, the value of R was found to change considerably when the tilted polarizer was rotated by 180° about the light-beam axis. The difference was attributed to a possible light-beam movement on the second polarizer due to bending of the light by Bi density inhomogeneities in the vapor cell. There would be a wavelength dependence of the bending because the refractive index of the vapor changes sharply with wavelength. The Oxford analysis of this effect predicts it will reverse when the polarizer is flipped 180°, and will go to zero when the polarizer face is normal to the light beam. In this case, the average of the two polarizer configurations above yielded the value $R = -(10.3 \pm 1.8) \times 10^{-8}$.

More recent measurements avoid the polarizer orientation problem by using a Glan-air polarizer with the analyzer polarizer face set normal to the beam axis to within 3×10^{-3} radian. These measurements give results consistent with the above average of tilted polarizer measurements.

A similar measurement to that described above at two points in the hyperfine structure which should have zero $\Delta\phi_{\mathrm{PNC}}$ gives a result of $R = -(0.2 \pm 1.4) \times 10^{-8}$. All the errors quoted are statistical and are one standard deviation.

The most recent published result [56] of the Oxford experiment is based upon an extensive series of measurements at the $6 \rightarrow 7$ hfs component and also at a nearby pair of points where $\Delta\phi_{\mathrm{PNC}}$ is also large and of reversed sign. During these measurements, the orientations of the oven, optical windows, and

polarizers were individually reversed relative to the light beam, and no systematic effect was revealed. The quoted result is

$$R_{\mathrm{exp}}(\mathrm{Bi}\ 648) = -(9 \pm 2) \times 10^{-8}\,. \tag{41}$$

4.4.2. The Novosibirsk experiment

Barkov and Zolotorev [36, 57, 58] at Novosibirsk have obtained results on several of the 648 nm M1 hyperfine components in bismuth using different techniques from those practiced in Oxford. The Novosibirsk group has placed much of their emphasis on atomic E2 and molecular bismuth test lines which should not give signs of PNC asymmetric rotation. In addition, the structure of the bismuth cell and the method of data acquisition are significantly different. The observed bismuth absorption pattern at 648 nm is shown in fig. 6. Most of the structure is due to Bi_2 molecular transitions. The M1 and E2 atomic lines are distinguished by Faraday rotation from the rest of the structure.

Figure 7 shows the version of the Novosibirsk experiment that was used to produce the data published thus far. The dye laser was a commercial device which was modified to permit a unique means of cavity mode selection. A tilted glass plate inside the laser cavity produced a reflection to a side arm, which acted as a Michelson interferometer and selected a single cavity mode. By displacing the reflecting mirror in the side arm, the laser output was tuned in discrete hops, as successive cavity modes

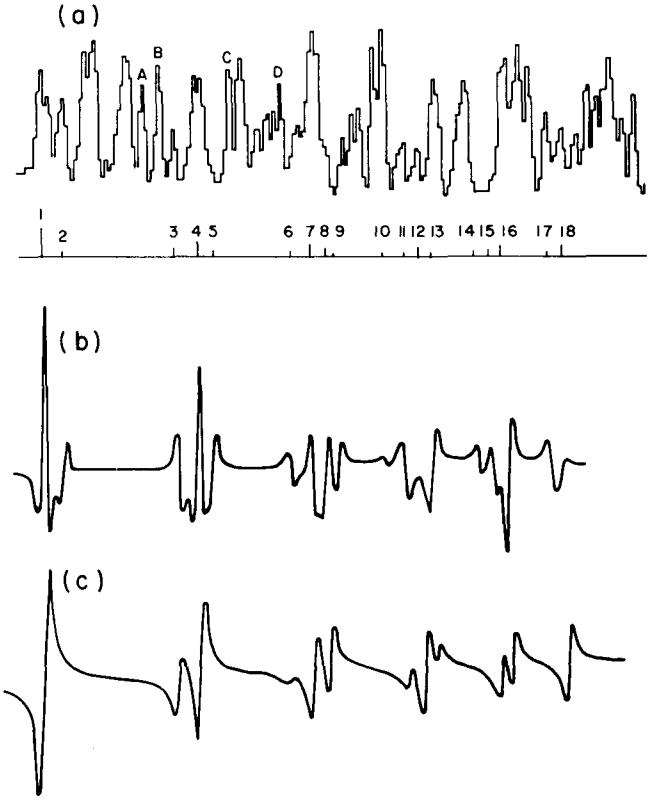

Fig. 6. Bismuth absorption and rotation curves at 648 nm. (a) Observed Novosibirsk absorption curve. (b) Theoretical Faraday rotation. (c) Theoretical parity rotation.

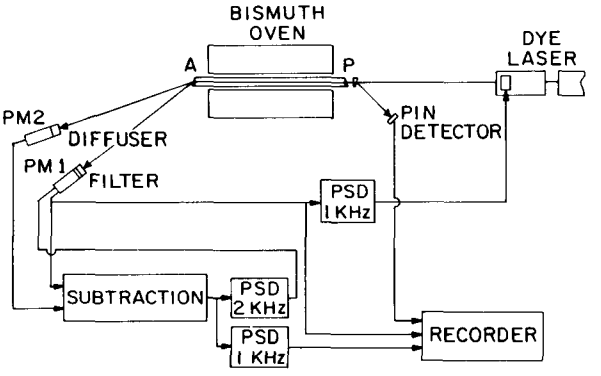

Fig. 7. Block diagram of the Novosibirsk PNC experiment.

(spaced about 416 MHz apart) were selected by the interferometer. Laser powers of about 2 mW were obtained in this manner. The absorption pattern at 648 nm displayed in fig. 6 shows the discrete tuning jumps.

A new version of the Novosibirsk experiment utilizes a commercial ring-laser with more power and wavelength stability than the earlier Novosibirsk laser. Other improvements have also been implemented. No results from this improved apparatus have appeared yet.

A heat pipe oven is used to produce the Bi vapor. When the oven is heated to about 1500 K, the Bi vapor pressure balances the He buffer gas pressure of about 2100 Pa (16 torr). The movement of Bi vapor outward from the center of the oven expels the helium gas, which then provides a barrier at either end of the oven where bismuth condenses and then returns to the center of the oven. A pool of liquid bismuth is maintained over the heated length of the tube. In order to act as a heat pipe the ends must be cooled to remove the heat carried by the bismuth vapor. The pressure of the bismuth vapor is easily regulated by controlling the applied helium pressure. This method establishes an effective path length through the vapor of about 50 cm. Running water cools a double layer magnetic shield which surrounds the oven. With the oven heaters off direct measurements of the magnetic field along the beam path give peak variations of less than 20 microgauss. A number of coils along the cell are used to produce axial magnetic fields which are used to measure the Faraday rotation and also map out the bismuth vapor distribution. These measurements are used to calibrate the bismuth optical depth. The Faraday rotation also serves to locate the M1 lines relative to the selected sweep ranges of the laser.

Calcite wedges which serve as the entrance and exit windows of the bismuth cell also act as polarizer and analyzer prisms. There are no additional glass windows between the polarizers to introduce spurious rotation into the system. This arrangement prevents the use of a Faraday rotation cell for rapid angle modulation. Instead the analyzing prism is rotated to settings of about 4×10^{-3} radian on either side of extinction. The uncompensated refraction by the polarizing prism determines the location of all subsequent optical components, and to avoid extensive realignment, one orientation of this prism has been maintained for all measurements.

The procedure for taking PNC data is to scan the laser at a 1 kilohertz rate across a selected M1 hyperfine component. Since the laser used when the data was taken did not scan frequency continuously, but rather hopped cavity modes, the frequency output was actually a step function with a sinusoidal envelope. Instead of transmitting only the rotated light, the analyzer prism refracts the light of each polarization into separate photomultiplier tubes. Diffusers at each detector make the detection

insensitive to movement associated with the modulation. The absorption pattern from PM1 (fig. 7) is fed through a 1 kHz PSD which corrects the laser frequency to keep the wavelength scan nearly centered on the absorption line. This feedback prevents a 1 kHz component of the absorption signal from appearing in the rotation signal from PM2 with a suppression factor of about 10^3. Because of the complicated Bi_2 absorption pattern overlaying the M1 and E2 lines, such a scan may not be symmetrical about the desired M1 line.

A 2 kHz PDS monitors the signal $V_s = (V_{PNC} - KV_{PM1})$ and adjusts the value of K in order to minimize the 2 kHz content in V_s. By thus equalizing the response of PM2 and PM1, the amount of 1 kHz present in V_s from the absorption signal is reduced further, by another suppression factor of about 10^3. Thus, the total suppression of 1 kHz from absorption is about 10^6, yielding an upper limit in the rotation signal of 10^{-9} rad. Finally, another 1 kHz PSD finds the parity signal contained in V_s, and relays that information to a computer-based data acquisition and control system. This controller normalizes the rotation signal for absorption and laser intensity changes. It also modulates the polarizer offset angle and simultaneously reverses the phase of the 50 Hz oven heater current. This latter action is intended to compensate for an observed systematic effect associated with the magnetic fields due to the oven currents.

PNC data was taken on a number of M1 hyperfine components, and compared with certain test lines (Bi_2 and E2 components) which should not show a PNC effect. The values of $\Delta\phi_{PNC}$ on the M1 components were used from those measurements in which a null result appeared on selected test lines with the idea that in those cases the size of the wavelength dependent background rotation pattern was a minimum. The results of the last round of published measurements at Novosibirsk, which do not include any of the measurements with the most recent apparatus, give a value [58]

$$R_{exp}(\text{Bi } 648) = -(20.1 \pm 3.2) \times 10^{-8}, \tag{42}$$

where the error is purely statistical. This result agrees with an earlier value $R = (-18 \pm 5) \times 10^{-8}$ [57] taken on basically the same apparatus, although with some changes having been effected since, such as a revised scheme for rotating the analyzing prism.

4.4.3. The Moscow experiment

Another experiment to measure optical rotation in bismuth has been underway since 1977 at the Lebedev Institute in Moscow [37, 59]. Their measurement method is similar to those described above, with some notable exceptions. Like the Novosibirsk group, the Moscow group uses single calcite prisms (wedges) which split the laser beam into two polarizations. A matched prism is used in front of the first polarizer to compensate for the net refraction in that polarizer. A Faraday cell is used between the polarizers to modulate the polarization angle. A single mode optical fiber is used to improve the spatial stability of the transmitted laser beam. A number of precautions have been taken to ensure that no optical surfaces between the polarizers will reflect light in such a way as to produce interference effects. The overall layout of the experiment is shown in fig. 8.

Modulation of the laser wavelength occurs between points of zero Faraday rotation on each side of the $F = 6 \rightarrow F = 7$ hfs line. The laser is also modulated to the maximum of the absorption line, which provides information about the size of the residual Faraday rotation. Magnetic shielding has not been used thus far.

The Moscow group has placed major emphasis on reducing the size of the wavelength-dependent

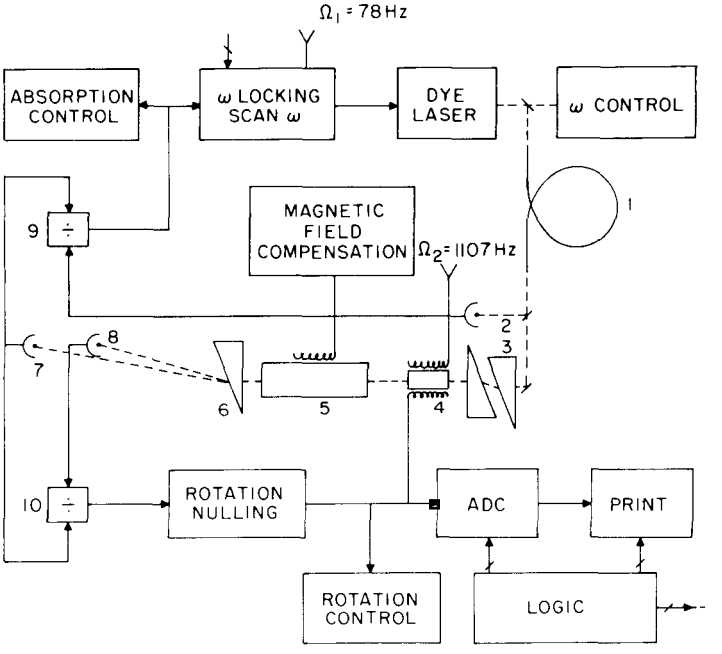

Fig. 8. Block diagram of the Moscow bismuth experiment.

background rotation pattern. The main contribution to this pattern that still remains in their experiment comes from interference effects due to multiple reflections inside the calcite prisms. They have advanced to the stage where the size of the pattern is reproducibly below 5×10^{-8} radian, which probably represents the current state of the art with birefringent materials.

The Moscow group obtained a value for R_{648} based upon several different bismuth densities. Their result is [59]:

$$R_{\mathrm{exp}}(\mathrm{Bi}\,648) = -(7.8 \pm 1.8) \times 10^{-8}\,, \tag{43}$$

where the uncertainty reflects both possible apparatus error and calibration errors.

4.5. *Measurements on the* 1.28 μm *line of atomic lead*

It has long been known that lead and thallium should have a PNC optical rotation at a level comparable to that in bismuth, yet the allowed magnetic dipole transitions in both elements fall near 1.28 μm, as shown for the case of lead in fig. 9. Only recently [60] have lasers been developed which can reach this wavelength. As at 876 nm, diode lasers now work handily at 1.28 μm. Therefore, the Seattle bismuth apparatus described in section 4.3.1 has been adapted to the longer wavelength with only minimal changes.

The InGaAsP/InP diode lasers at 1.28 μm have remarkably similar characteristics to the GaAlAs lasers used in the Bi experiment. Carbon disulfide proved to be an effective medium for the Faraday rotator at 1.28 μm. Optical detection is accomplished with liquid nitrogen cooled Ge diodes.

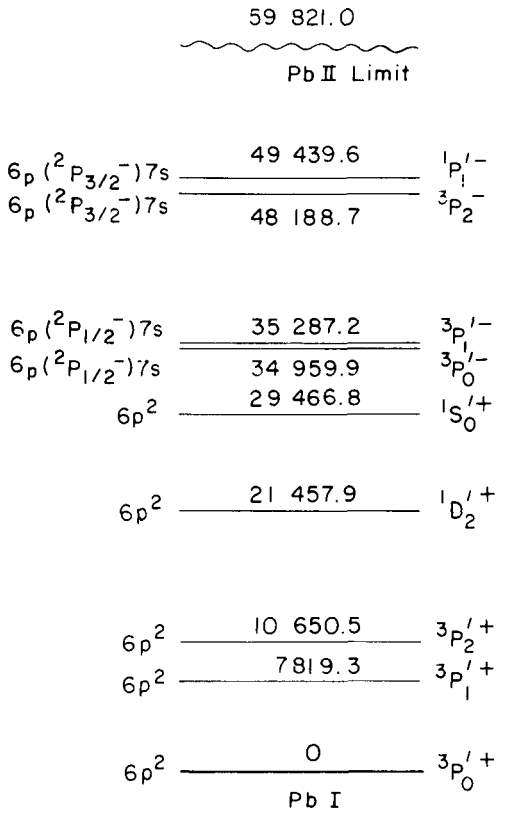

Fig. 9. Atomic lead energy levels.

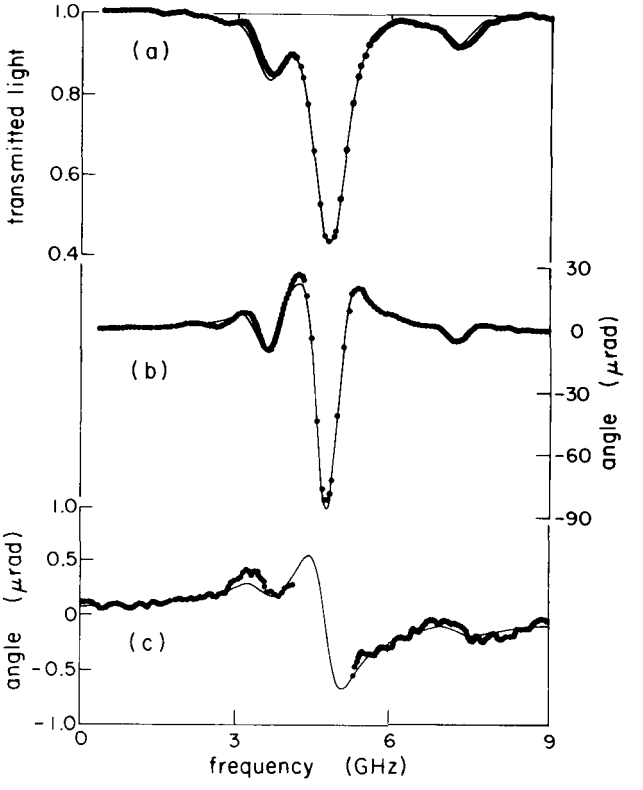

Fig. 10. Rotation and transmission curves in atomic lead at 1.28 μm. Solid curves are theory and points are data from the Seattle experiment. (a) Transmission. (b) Faraday rotation. (c) Parity rotation.

The first measurements with this modified apparatus have been made on the $J = 0 \rightarrow J = 1$ Pb transition at 1.2788 μm. Naturally occurring lead is used, which has 22% ^{207}Pb having a two-component hfs structure, and 78% even isotopes with no hfs structure. The observed absorption pattern and Faraday rotation are shown in fig. 10, together with the expected theoretical curves.

At comparable temperatures, the M1 absorption on the even isotope line in Pb is 10 times greater than on the largest hfs component at 876 nm in Bi. This allows operation at lower temperatures where the system is more stable, or alternatively at higher absorption lengths where the PNC rotation is larger.

Table 3 shows results of PNC data taken at several oven temperatures corresponding to a range from 10 to 75 absorption lengths on the even isotope line. Both Glan–Thompson and Nicol polarizers were used. There is agreement among the six separate measurements within their uncertainties. Figure 10c shows the PNC data from measurement 1, and reveals the expected PNC dispersion shape. The systematic tests and controls described in section 4.3.1 have been utilized with all lead data. PNC data points on the transmission minima are omitted because of the difficulty of normalizing the data correctly at such low light levels.

The data in table 3 yields the value [61]

$$R_{\mathrm{exp}}(\mathrm{Pb}\ 1.280) = -(9.9 \pm 2.5) \times 10^{-8}, \tag{44}$$

Table 3
Seattle measurements of $R = \mathrm{Im}(\mathscr{E}_{\mathrm{PNC}}/\mathscr{M})$ in lead (1.279 μm)

Optical depth	Polarizers	$10^8 R$	Stat. error ($\times 10^8$)	Sys. error ($\times 10^8$)
8.5	GT[a]	−15.54	4.0	2.6
50	GT	−9.05	1.3	1.5
80	N[b]	−2.78	8.1	3.9
25	N	−10.03	2.8	1.9
75	N	−11.53	3.0	1.6
15	GT	−8.33	3.6	2.5
	Wt. av.	-9.9 ± 2.5[c]		

(a) Glan–Thompson polarizer.
(b) Nicol polarizer.
(c) Some systematic errors are random between data groups while others are not. This final error takes this into consideration.

where the quoted error is mainly a composite of residual systematic uncertainties. There is agreement with the theoretical value in eq. (38) within the uncertainties in both the experiment and theory.

5. PNC-Stark experiments using twice-forbidden M1 transitions

5.1. Overview

In their original paper, Bouchiat and Bouchiat [15] presented a very clever experimental approach which would utilize highly forbidden M1 optical transitions in heavy elements such as Cs and Tl. Such experiments were undertaken at Paris using Cs and at Berkeley using Tl. Both groups have reported observations of PNC signals. More recently, Cs experiments were also undertaken at Zurich [62, 63] and at Michigan [64], although they have not yet achieved the accuracy needed to observe parity nonconservation.

The optical energy levels of Cs and Tl are shown in fig. 11. The transitions used are $6^2S_{1/2} \rightarrow 7^2S_{1/2}$ at 539 nm in Cs and $6^2P_{1/2} \rightarrow 7^2P_{1/2}$ at 293 nm in Tl. In the nonrelativistic approximation, these are each

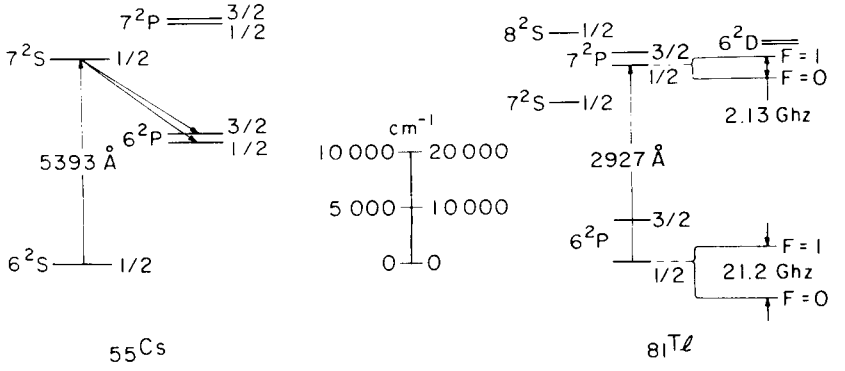

Fig. 11. Cesium and thallium energy levels.

forbidden to M1 because the radial quantum number changes. Spin–orbit coupling and other relativistic effects permit these transitions to take place, but with an M1 moment amplitude of order α^2 times the Bohr magneton.

The original concept was to look for a circular polarization dependence (circular dichroism) in the M1 transitions through E1–M1 interference, with a strong enhancement of the fractional effect in eq. (10) because of the exceedingly tiny M1 amplitude. The idea was to monitor the fluorescence from the upper state when a vapor of the atoms was illuminated with circularly polarized light at the M1 transition wavelength. Changes in the intensity of the fluorescence accompanying changes in the sense of circular polarization of the incident light would measure the PNC effect. Fractional effects as large as 10^{-4} in Cs and 10^{-3} in Tl might be expected.

In practice, because the M1 transitions are so weak, other sources of background light are too large compared to the desired fluorescence for the experiments to be feasible in the original concept. However, the transitions can be observed readily by Stark mixing using a static electric field E_s. This gives a PNC-Stark interference of the form of eq. (15). While the useful signal is increased as E_s^2, the fractional PNC effect is reduced in proportion to the size of E_s. The electric fields required to raise the signals above background lead to expected fractional PNC effects of order 10^{-6}–10^{-5} for Cs and Tl.

5.2. *Atomic calculations in thallium and cesium*

The central field IPM model discussed in section 4.2.1 should provide a better approximation for the transitions here than for the Bi and Pb transitions. In particular, the effect of shielding (section 4.2.5) should be small, whereas it is the major correction to the central field result in bismuth.

In the case of Cs, shielding is small because the core electronic shells are extremely rigid. In the case of Tl, the $6s^2$ core electrons are actually highly polarizable and could in principle shield the PNC amplitude associated with the 6p electron shell. However, the PNC effect on the transition of interest, $6^2P_{1/2} \rightarrow 7^2P_{1/2}$ involves contributions from both levels and it happens that the PNC admixture is considerably larger in the upper state, due to the proximity of the even parity $7^2S_{1/2}$ and $8^2S_{1/2}$ states. Because the wave functions overlap much further out, matrix elements involving $n \geq 7$ states are affected much less by core polarization than are 6p–6s matrix elements. The effect of shielding is probably less than 10%.

It should be noted that the overlap argument would indicate a sizable shielding contribution in the case of the $6^2P_{1/2} \rightarrow 6^2P_{3/2}$ transition in Tl that is being studied by optical rotation.

5.2.1. *Thallium calculation*: $6^2P_{1/2} \rightarrow 7^2P_{1/2}$

Calculations of PNC on this Tl transition have been carried out by Bouchiat and Bouchiat [32], Neuffer and Commins [65], Sushkov, Flambaum and Khriplovich [66], and Das et al. [67]. All of the calculated results are approximately the same size, although they are arrived at by varying methods. The first three sets of authors use one-electron central field (OECF) methods of solving the problem similar to the central field IPM of section 4.2.1. In particular, Neuffer and Commins iteratively solve the one-electron Dirac equation in a "modified Tietz potential", with parameters chosen to yield agreement (0.1%) with the observed $6^2P_{1/2}$ and $7^2P_{1/2}$ levels. Other low-lying states are then obtained to within 2%. Tests of this model were made by comparison with experimental and other theoretical fine structure, hyperfine structure, and some allowed E1 transition rates. No serious discrepancies were found. The comparisons with hfs are of particular interest because they test the wave function near the origin. The

agreement of Neuffer and Commins' results with other calculations based upon OECF models led them to attribute small discrepancies to admixtures of configurations which do not affect PNC calculations. The agreement among authors, and the good predictions (within 20%) of most observed E1 transitions lend confidence to the OECF model, and affirm the smallness of core polarization effects for this particular calculation.

The 6s–6p transition was not included in the above tests by Neuffer and Commins. It was included in the work of Sushkov et al., and as already noted in section 4.2, a serious discrepancy was found. However, the contribution of the 6s–6p matrix element to PNC for the Berkeley experiment was found by Sushkov et al. to be small.

Neuffer and Commins used their parametric potential to evaluate eq. (1) and found the result $\mathscr{E}_{\mathrm{PNC}} = 1.93\mathrm{i} \times 10^{-10} Q|\mu_{\mathrm{B}}|$, where Q is given by eq. (23). Sushkov et al., applying the semi-empirical approach, found $\mathscr{E}_{\mathrm{PNC}} = 1.80\mathrm{i} \times 10^{-10} Q|\mu_{\mathrm{B}}|$. Bouchiat and Bouchiat obtained an estimate of $\mathscr{E}_{\mathrm{PNC}} = 1.48\mathrm{i} \times 10^{-10} Q|\mu_{\mathrm{B}}|$.

Das et al. used relativistic many-body perturbation theory (RMBPT) to calculate $\mathscr{E}_{\mathrm{PNC}}$ for the $6^2\mathrm{P}_{1/2} \rightarrow 7^2\mathrm{P}_{1/2}$ transition in Tl. Their method is similar to the Oxford treatment of bismuth discussed in section 4.2. They evaluated four types of terms which contribute to $\mathscr{E}_{\mathrm{PNC}}$: a direct term (e.g., PNC mixing of the $6\mathrm{P}_{1/2}$ state to nS states, and then coupling by the usual electric dipole to the $7\mathrm{P}_{1/2}$), an indirect term (PNC mixing of the $6\mathrm{P}_{1/2}$ to the 6S and then coupling through E1 to the $7\mathrm{P}_{1/2}$), a consistency term (electron–electron exchange interaction), and a correlation term (pair-correlations). The first two terms constitute a zero-order calculation equivalent to the calculation of Neuffer and Commins. Das et al. obtain a zero-order value $\mathscr{E}_{\mathrm{PNC},0} = 2.06\mathrm{i} \times 10^{-10} Q|\mu_{\mathrm{B}}|$. The two correction terms decrease the size of the effect to the final result of Das et al., $\mathscr{E}_{\mathrm{PNC}} = \mathrm{i}(1.51 \pm 0.07) \times 10^{-10} Q|\mu_{\mathrm{B}}|$. We take the average of the three most recent calculations [65, 66, 67] for our best theoretical value:

$$\mathscr{E}_{\mathrm{PNC}} = 1.75\mathrm{i} \times 10^{-10} Q|\mu_{\mathrm{B}}| \,. \tag{45}$$

Das et al. ascribe a fairly small uncertainty (5%) to their calculation, but they believe that a calculation accurate to 2% could also be made by including higher-order terms. As we will see, the usefulness of the prediction is presently limited by uncertainties in the experimental results and by uncertainties in a companion calculation of Stark amplitudes needed for interpreting the experimental results.

A still more difficult and uncertain task is the theoretical calculation of the M1 transition rate. Neuffer and Commins [65] obtain a value of $\mathscr{M} = -(3.2 \pm 1.0) \times 10^{-5} |\mu_{\mathrm{B}}|$. However, a theoretical value of $\mathscr{M}$ is not used for interpreting the measurement of PNC circular dichroism. Instead, the M1 interference with a calculable Stark amplitude is determined experimentally. Chu, Commins and Conti [18] have measured the amplitude in this way and found:

$$\mathscr{M} = -(2.1 \pm 0.3) \times 10^{-5} |\mu_{\mathrm{B}}| \,. \tag{46}$$

This value of $\mathscr{M}$ is used for making comparisons between calculations of $\mathscr{E}_{\mathrm{PNC}}$ and the measurements of circular dichroism through Stark interference.

At present, the weakest link in the theoretical treatment of Tl, and the most serious need, is understanding the Stark amplitude between the two states. It is likely that the electric field mixing of the 6p state with s and d states will be subject to similar corrections to those incorporated into the PNC effect [67]. Since knowing the Stark amplitude is crucial to the actual PNC measurement, as will be evident in the experimental discussion below, some attention will be focused on this issue here.

The Stark mixing in lowest (OECF) order has been calculated by Neuffer and Commins with the same potential used for PNC. There are some computational differences between the Stark and PNC calculations, however. H_{PNC} is a pseudoscalar, and hence does not mix different j. $H_{\mathrm{S}} = eE_{\mathrm{S}} \cdot \boldsymbol{r}$ is a vector and does mix j with $j \pm 1$. Also S and D states are admixed with the P-states.

For reference we include here rather detailed results of the Stark mixing. Let θ_{s} be the angle between the light beam plane of polarization and E_{S}. Then the Stark-induced E1 transition amplitude of eq. (14) can be represented by the 2×2 matrix

$$\langle 7^2\mathrm{P}_{1/2} m'_J(\mathrm{Stark}) | \hat{E}1 | 6^2\mathrm{P}_{1/2} m_J(\mathrm{Stark}) \rangle = E_{\mathrm{s}} x \tag{47}$$

$m'm_J$	$\frac{1}{2}$	$-\frac{1}{2}$
$\frac{1}{2}$	$\alpha \cos\theta_{\mathrm{s}}$	$-\mathrm{i}\beta \sin\theta_{\mathrm{s}}$
$-\frac{1}{2}$	$-\mathrm{i}\beta \sin\theta_{\mathrm{s}}$	$\alpha \cos\theta_{\mathrm{s}}$

where

$$\alpha = \frac{1}{9}\sum_{n\mathrm{S}} R_{7\mathrm{P},n\mathrm{S}} R_{6\mathrm{P},n\mathrm{S}} \left(\frac{1}{E_{7\mathrm{P}} - E_{n\mathrm{S}}} + \frac{1}{E_{6\mathrm{P}} - E_{n\mathrm{S}}} \right) + \frac{2}{9}\sum_{n\mathrm{D}_{3/2}} R_{7\mathrm{P},n\mathrm{S}} R_{6\mathrm{P},n\mathrm{S}} \left(\frac{1}{E_{7\mathrm{P}} - E_{n\mathrm{D}}} + \frac{1}{E_{6\mathrm{P}} - E_{n\mathrm{D}}} \right) \tag{48}$$

and

$$\beta = \frac{1}{9}\sum_{n\mathrm{S}} R_{7\mathrm{P},n\mathrm{S}} R_{6\mathrm{P},n\mathrm{S}} \left(\frac{1}{E_{6\mathrm{P}} - E_{n\mathrm{S}}} - \frac{1}{E_{7\mathrm{P}} - E_{n\mathrm{S}}} \right) + \frac{1}{9}\sum_{n\mathrm{D}_{3/2}} R_{7\mathrm{P},n\mathrm{D}} R_{6\mathrm{P},n\mathrm{D}} \left(\frac{1}{E_{7\mathrm{P}} - E_{n\mathrm{D}}} - \frac{1}{E_{6\mathrm{P}} - E_{n\mathrm{D}}} \right), \tag{49}$$

with $R_{7\mathrm{P},n\mathrm{S}} = \langle 7^2\mathrm{P}_{1/2} | er | n^2\mathrm{S}_{1/2} \rangle$ and the remaining notation self-evident. Neuffer and Commins evaluated the sums both by explicitly evaluating contributions of nearby levels and by using a Green's function method [65] to execute the complete sums.

Only further Clebsch–Gordan algebra is required to include hyperfine structure. The complete dipole transition matrix has been tabulated elsewhere [8, 65].

Work continues on improving the evaluation of α and β [68]. Both an empirical approach utilizing measured transition amplitudes and a thoroughgoing many-body approach to include shielding and other correlations could be useful. At this stage, uncertainties in α and β may be at the ± 20 % level in Tl.

Interference between the PNC and Stark mixing amplitudes can be observed by shining circularly polarized light on the sample and detecting the polarization of the $7^2\mathrm{P}_{1/2}$ state given by eq. (15). If we add the M1 contributions as well to the right-hand side of eq. (15) we obtain an expression true for large electric fields ($E_{\mathrm{S}} \gg 1$ V/cm):

$$P_z \equiv \boldsymbol{P}_{\mathrm{e}} \cdot \hat{\boldsymbol{k}} \times \hat{\boldsymbol{E}}_{\mathrm{s}} = (\mathcal{M} + \eta \mathscr{E}_{\mathrm{PNC}})/\mathscr{E}_{\mathrm{s}}(F, F') \tag{50}$$

where $\mathscr{E}_{\mathrm{s}}$ is a measure of the Stark-induced amplitude given in terms of α, β, and the field E_{S}, and

depends upon the initial and final hyperfine states F and F'. For certain transitions in Tl [65]:

$$P_z(F=0\rightarrow F=0)=0$$
$$P_z(F=0\rightarrow F=1)=-2(\mathcal{M}+\eta\mathcal{E}_{\mathrm{PNC}})/\beta E_{\mathrm{S}}\,, \tag{51}$$

where again the approximation is valid for large E_{S}.

5.2.2. Cesium

From a theoretical point of view, Cs is especially attractive. As an alkali metal, it contains one valence electron outside of a "noble gas" core which is probably quite rigid against polarization. Bouchiat and Bouchiat [15] first proposed looking for PNC in heavy elements, and Cs was their first choice. The transition involved is the $6^2S_{1/2}\rightarrow 7^2S_{1/2}$.

The M1 transition is forbidden: It can proceed only by spin flip (the $\boldsymbol{S}$ term in eq. (6)), but the radial wave functions are orthogonal. In order to calculate a nonvanishing transition amplitude, higher-order effects must be invoked. These include retardation, relativistic corrections, core polarization, etc. Bouchiat and Bouchiat estimated the reduced matrix element to lie between 10^{-5} and 10^{-4} atomic units, and as discussed below, it has since been measured. However, as in the case of Tl, the search for PNC-induced E1 interference with M1 has been abandoned in favor of a search for PNC-Stark interference.

The calculations of $\mathcal{E}_{\mathrm{PNC}}$ in Cs are straightforward and should be the most reliable of the heavy atoms being studied. Bouchiat and Bouchiat employed a clever variation of the Fermi–Segré method [31]. Loving and Sandars [69] used a parametric potential. More recently very thorough and systematic calculations have been carried out [70], giving the value for the $6^2S_{1/2}$ to $7^2S_{1/2}$ transition of

$$\mathcal{E}_{\mathrm{PNC}}=\mathrm{i}(3.42\times 10^{-11})Q|\mu_{\mathrm{B}}|=\mathrm{i}(0.85\times 10^{-11}ea_0)\,. \tag{52}$$

A summary of calculations of $\mathcal{E}_{\mathrm{PNC}}$ for both Cs and Tl is given in table 4.

The calculation of the Stark amplitude between the 6S and 7S states should be reliable also. Shielding and other correlation effects are expected to be very small because of the inert core. As in Tl (eqs. (47)–(49)) there are the scalar and vector polarizabilities α and β; however, in Cs only mixing between s and p states contributes. The calculated values are [62–64, 70]

$$\alpha=-258a_0^3\,,\qquad \beta=27a_0^3\,. \tag{53}$$

A semi-empirical value of α and precise measurements of β/α by several groups [62, 64, 71] lead to a semi-empirical value of β which is in very good agreement with the theoretical value above.

As in Tl (eqs. (50), (51)), the experimentally measured quantity is the polarization P_{e} induced in the excited state through Stark-PNC interference and other interference effects. In the case of Cs, for a $\Delta F=0$ transition between s states, the correct expression for this polarization is [32, 73]:

$$\boldsymbol{P}_{\mathrm{e}}=-\frac{8}{3}\frac{F(F+1)}{(2I+1)^2}\left\{(\mathcal{M}+\eta\mathcal{E}_{\mathrm{PNC}})\frac{\hat{\boldsymbol{k}}\times\hat{\boldsymbol{E}}_{\mathrm{s}}}{\alpha E_{\mathrm{s}}}-\eta\frac{\beta}{\alpha}\boldsymbol{k}\right\}, \tag{54}$$

where the notation is the same as in eqs. (15, 50, 51), and I is the nuclear spin. Here we have displayed

Table 4
Theoretical values of PNC quantities in thallium and cesium. $Q = Z(1 - 4\sin^2\theta_w) - \eta$

Transition (nm)	$\mathrm{Im}(\mathscr{E}_{PNC}/\lvert\mu_B\rvert)$	$\delta = 2\,\mathrm{Im}(\mathscr{E}_{PNC}/\mathscr{M})$[a]	$\mathrm{Im}(\mathscr{E}_{PNC}/\beta)$[b]	Method
Tl (293)	$1.93\times10^{-10}Q$	$-9.2\times10^{-6}Q$		Modified central potential[c]
	$1.78\times10^{-10}Q$	$-8.5\times10^{-6}Q$		Semiempirical[d]
	$1.37\times10^{-10}Q$	$-6.5\times10^{-6}Q$		Fermi–Segré central potential[e]
	$1.51\times10^{-10}Q$	$-7.2\times10^{-6}Q$		RMBPT[f]
Cs (539)	$4.7\times10^{-11}Q$		$0.0323Q$ mV/cm	Fermi–Segré central potential[e]
	$4.0\times10^{-11}Q$		$0.0275Q$ mV/cm	Parametric potential[g]
	$3.42\times10^{-11}Q$		$0.0235Q$ mV/cm	Many-body corrections and screening[h]

(a) While δ is not measured directly, it is frequently quoted as the experimental result. To calculate δ, we use the experimental value of $\mathscr{M}$ from ref. [18].

(b) The experimental quantity in Cs depends upon β, the vector polarizability in eq. (53). Here we use the value of β calculated in ref. [70].

(c) Ref. [65]. (f) Ref. [67].
(d) Ref. [66]. (g) Ref. [69].
(e) Ref. [32]. (h) Ref. [70].

the M1 and PNC interference with the Stark amplitude which produces the $\boldsymbol{k}\times\hat{\boldsymbol{E}}_s$ component, and have shown also the component along $\hat{\boldsymbol{k}}$ due essentially to optical pumping by the circularly polarized light along $\hat{\boldsymbol{k}}$. This latter term is used to calibrate the transition rate and polarization efficiency in the Paris experiment, and is also important as a source of certain potential systematic effects.

5.3. *Cesium experiment* [71–73]

The experiment at Paris was the first one conceived in order to take advantage of the enhancement of PNC effects in heavy atoms. The $6^2S_{1/2}\rightarrow 7^2S_{1/2}$ forbidden M1 transition in cesium (fig. 11) has been used from the beginning. The 539 nm radiation required for this transition is readily produced with modern dye lasers, and the 1.36 μm fluorescence from $7^2S_{1/2}\rightarrow 6^2P_{1/2}$ can be efficiently detected with solid-state devices now available.

The electronic polarization $\boldsymbol{P}_e$, shown in eq. (54), is induced in a cesium vapor by absorption of circularly polarized laser light in the presence of the static electric field $\hat{\boldsymbol{E}}_s$. The circular polarization of the 1.36 μm fluorescence serves to measure $\boldsymbol{P}_e$. As is evident from eq. (54), the part of $\boldsymbol{P}_e$ due to the PNC interaction may be measured by determining the change in circular polarization of the fluorescence radiation along the direction $\hat{\boldsymbol{k}}\times\hat{\boldsymbol{E}}_s$ when the circular polarization η of the incident light along $\hat{\boldsymbol{k}}$ is reversed. Reversal of $\boldsymbol{E}_s$ further distinguishes the PNC term.

In the Paris experiment, light-polarization modulations described further on in this section [72] give all atomic signals specific labelings, eliminating all background signals. There is background noise, the main sources of which are black body radiation from the Cs oven and light scattering from dimers and other constituents of the Cs vapor. One increases E_s until the photon noise in the light scattered in the Stark-induced transition dominates over the background noise but not so much that the fractional polarization change in η becomes so small that other systematics become significant. Once the Stark-induced fluorescence dominates, the fundamental shot noise limit does not change with E_s, because the fractional polarization change and the fractional shot noise each vary as E_s^{-1}, i.e. as the

inverse square root of the counting rate. The size of E_s here plays a similar role to that of the angle of offset of the polarizer from extinction in the optical rotation experiments.

In Cs the Stark transition has the same rate as the M1 transition when $E_s = (2.62 \pm 0.21)$ V/cm [73]. In order to raise the 7s→6p fluorescence rate above background, the Paris group operates with $E_s \sim$ 100 V/cm. Thus, from eqs. (51–53), $\Delta P_e \sim 3 \times 10^{-6}$ is expected in Cs due to PNC.

The Paris experimental arrangement is given in fig. 12. Cs atoms at a pressure of about 13 Pa (0.1 torr) are excited by a single-mode c.w. dye laser which produces about 0.5 watt at the 6s→7s transition frequency.

Within the Cs vapor cell are two parallel plates between which the $\boldsymbol{E}_s$ field is applied, and two spherical mirrors which reflect the laser beam repeatedly through the Cs vapor, increasing the 7s→6p fluorescence signal and precisely reversing the sign of η upon each reflection. Note that the circular polarization vector $\eta\hat{\boldsymbol{k}}$ does *not* change upon reflection, and hence the PNC term in eq. (54) remains unchanged. The change in polarization is $<10^{-5}$ per reflection. The experiment operates with about 70 double passes of the laser beam, which increases the signal by a factor of over 100.

The multiple-pass scheme not only increases the signal size, but as a result of the beam reversal also cancels a number of systematics. The $\mathcal{M}$ term in P_e reverses with each reflection, since it is proportional to $\hat{\boldsymbol{k}}$, resulting in an approximate cancellation of this source of polarization and of systematics associated with M1, for an even number of reflections. The cancellation is only approximate because of reflection losses of the laser beam and changes in beam position. Nevertheless, the M1 polarization term is reduced by a factor greater than 100. This is important, since the size of $\mathcal{M}$ in eq. (54) is about 10^4 times the size of $\mathcal{E}_{PNC}$, and without the cancellation a great burden is put on reversing η without undue side effects. Another important cancellation is the removal of magnetic field systematics. With such a large number of reflections, an 80 gauss magnetic field is required to mimic the size of effect predicted by the W-S model.

The infrared detector is a pure Ge crystal cooled to LN_2 temperatures in order to reduce detector noise, and is contained within a lead-lined box in order to reduce noise originating in detection of cosmic rays. The collection optics gather approximately 0.1 steradian of the emitted radiation, and include an interference filter centered at 1.36 μm. This filter has a peak transmission of about 60 % with a 4.5 nm bandwidth. The 8 cm diameter of the filter, while large for such filters, is small enough to limit the ability of the optics to spatially filter the fluorescent light from other sources of light, such as black body radiation from the Cs oven, so that great care must be taken with oven design.

The PNC polarization is measured by detecting the fluorescence along the $\hat{\boldsymbol{k}} \times \boldsymbol{E}_s$ direction through a rotating $\frac{1}{4}$-wave plate and a fixed plane-polarizing sheet, providing a modulation in circular analyzing power at frequency ω_f.

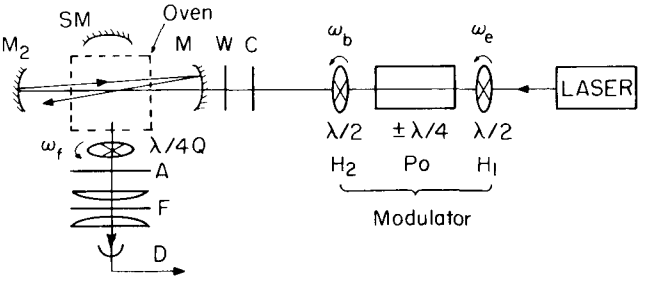

Fig. 12. Block diagram of the Paris cesium experiment.

The circular polarization of the incident beam is created by passing a plane-polarized laser beam through a $\pm\lambda/4$ Pockels cell between two $\lambda/2$ plates. The $\lambda/2$ plates rotate at different frequencies, $\omega_b/4$ and $\omega_e/4$, to produce a linear polarization rotating at frequency ω_b and a circular polarization, both having amplitude modulation at frequency ω_e. By using phase-sensitive detection at different combinations of ω_e, ω_b and ω_f, specific labels of circular polarization and linear polarization effects are obtained with negligible cross-modulation. The PNC effect, which changes with incident circular polarization, is proportional to $\eta[\sin(\omega_e+\omega_f)t-\sin(\omega_e-\omega_f)t]$, which has continuous sinusoidal modulations and a discrete modulation due to η reversal by the Pockels cell. Important systematic effects due to asymmetry in polarization reversal can be estimated from the behavior of the linear polarization modulation.

Another class of systematic effects can come from imperfect electric field reversal coupled with a lack of complete orthogonality among the beam, field, and detection directions. For example, if there is a nonreversing stray electric field acting on the atoms, with a component along the pump laser beam, then P_e acquires a dependence on η. A series of auxiliary measurements [74] enables this systematic to be reduced and its size estimated.

These and other expected systematic perturbations are reduced as much as possible and then are carefully monitored. Various consistency checks are used to guard against any unexpected systematic effects.

The $\mathscr{E}_{PNC}$ term of eq. (54) is calibrated against the β/α term of the same equation. This latter term, the component of $\boldsymbol{P}_e$ along $\hat{\boldsymbol{k}}$, usually does not appear in the observation direction $\hat{\boldsymbol{k}}\times\hat{\boldsymbol{E}}_S$. However, a component of this term is rotated into the observation direction by a large magnetic field that is periodically applied parallel to $\boldsymbol{E}_S$. The rotated fraction of this polarization is readily calculable from the calibrated magnetic field, and is easily distinguished since it is invariant under $\boldsymbol{E}_S$ reversal. The ratio of the $\mathscr{E}_{PNC}$ term to the β/α term is the experimental quantity of interest. Note that the circular analyzing power, laser intensity, and other factors in the overall sensitivity drop out in this ratio and one is left with a pure measurement of $\mathscr{E}_{PNC}/\beta$.

Most of the operation of the experiment, as well as the data processing, is electronically automated. The calibration magnetic field is switched on periodically, while PNC data collection and systematic checks are carried out in between. The system controller also monitors the equality of $\pm E_S$, adjusts a compensating magnetic field to minimize the detected component of the large calibration β/α term of eq. (54) during PNC data acquisition, rejects noise peaks in the PNC data, and averages the PNC data over 80-second intervals.

After 300 hours of PNC data integration time (over 500 hours of real operation time including dead time and auxiliary measurements) the Paris experiment yielded the result [72] on the $\Delta F=0$ $(4\rightarrow 4)$ hyperfine component:

$$\begin{aligned}&\mathrm{Im}\,\mathscr{E}_{PNC}/\beta=-1.34\pm0.22\ \text{or}\ (\sim0.11)\ (\text{in mV/cm}),\\&\mathrm{Im}\,\mathscr{E}_{PNC}=[0.71\times10^{-11}\pm0.11\pm(\sim0.05)]ea_0=[1.9\times10^{-9}\pm0.3\pm(\sim0.14)]\mu_B\end{aligned}\tag{55}$$

in terms of the electronic charge, e, Bohr radius, a_0, and Bohr magneton, μ_B. The second expression uses the calculated value [70] of β, with any theoretical error in this calculation ignored. In each expression, the first listed uncertainty is statistical and is accounted for by shot noise in the detected photons. The second uncertainty, listed in parentheses, is the estimated uncertainty due to known sources of error. A systematic correction of 0.04 has been applied.

Continued advances in the Cs experiment are quite likely. The Paris group expects to employ a new method utilizing an external magnetic field along $\hat{\boldsymbol{k}} \times \hat{\boldsymbol{E}}_s$ sufficiently large to permit optical resolution of the Zeeman components of the absorption line. The intensity of the fluorescence rather than its circular polarization becomes the detected signal, which allows a large increase in the signal size. The PNC signal is odd under reversal of the incident circular polarization, the electric field, and the magnetic field; i.e., the measured pseudoscalar is $\eta \hat{\boldsymbol{k}} \times \hat{\boldsymbol{E}}_s \cdot \hat{\boldsymbol{B}}$.

Other experiments on Cs were mentioned already, one at Zurich [63] and a yet more recent effort at Michigan [64], the latter utilizing a transverse Cs beam to obtain sub-Doppler resolution. These experiments are expected to yield useful results in the near future.

A second measurement of PNC on the 6S–6P transition in cesium has been completed recently at Paris [71], this time using a $\Delta F = 1$ hyperfine component rather than the $\Delta F = 0$ component described above. Most of the important measured quantities and possible systematic effects differ between these two hyperfine components. The result of this second measurement is [71]:

$$\begin{aligned} &\mathrm{Im}\, \mathscr{E}_{\mathrm{PNC}}/\beta = -1.78 \pm 0.26 \pm (\sim 0.12)\ (\text{in mV/cm}) \\ &\mathrm{Im}\, \mathscr{E}_{\mathrm{PNC}} = 0.94 \times 10^{-11} e a_0 \,. \end{aligned} \tag{56}$$

The theoretical value in eq. (52) agrees with each of the experimental values above and is in excellent agreement with the average experimental value.

5.4. Thallium experiment

As mentioned already, this experiment is similar in concept to the Paris experiment with cesium. The $6P_{1/2}$–$7P_{1/2}$ transition in atomic Tl is used, which falls in the UV at 293 nm and can be reached by frequency doubling the visible output of a pulsed tunable dye laser. The smaller average intensity available from such a light source is compensated by the larger $\mathscr{E}_{\mathrm{PNC}}$ amplitude in Tl compared with Cs because of the larger Z. As with Cs, the PNC-Stark interference is measured by driving the transition with circularly polarized light in the presence of a static electric field, and observing electronic polarization P_z that is produced in the excited state, as given by eq. (51).

At Berkeley a new method to measure P_z has been exploited. The $7P_{1/2}$ atoms are pumped to the $8S_{1/2}$ state by a 2.18 μm (IR) circularly polarized laser beam directed along $\boldsymbol{k}_{\mathrm{UV}} \times \boldsymbol{E}_s$, and the intensity $I_{+,-}$ of the $8S_{1/2}$–$6P_{3/2}$ fluorescence is monitored as the 2.18 μm circular polarization $\eta_{\mathrm{IR}} = \pm 1$ is changed. Using the customary alignment of axes, $\boldsymbol{k}_{\mathrm{UV}}$ and $\boldsymbol{E}_s$ are parallel to x and y respectively, and P_z is to be measured. The asymmetry

$$A_0 \equiv (I_+ - I_-)/(I_+ + I_-) = 0.7 P_z \tag{57}$$

is the measured quantity, and is the sum of asymmetries A_0^{M} and A_0^{PNC} due to M1 and E1 respectively. Note that by eq. (51), A_0^{M} is odd under $\boldsymbol{E}_s$ reversal, while A_0^{PNC} is odd under both $\boldsymbol{E}$ and η_{UV} reversal. Thus, care must be taken that reversing η_{UV} does not cause any changes that would change the contribution of M1 to P_z. The dilution factor 0.7 above may be calibrated by directing the IR beam along x and measuring the large and known value of P_x proportional to η_{UV}. Alternatively, the ratio $\mathscr{E}_{\mathrm{PNC}}/\mathscr{M}$ may be determined independently of calibration by measuring A^{M} and A^{PNC} at the same time.

The use of laser pumping to measure P_z offers some advantages over the alternative of measuring the

circular polarization of the fluorescence from the $7P_{1/2}$ state. The $7P_{1/2}$–$7S_{1/2}$ fluorescence is at a wavelength of poor detection sensitivity and high black body background, while fluorescence from $7S_{1/2}$ to $6P_{3/2}$ suffers from cascade depolarization and resonance trapping. Further, the need to measure circular polarization imposes a limit on the usable solid angle of detection. Finally, laser pumping allows the fluorescence to be displaced to a quieter part of the spectrum.

The Berkeley apparatus is shown schematically in fig. 13. L1 is a flash-lamp pumped tunable pulsed dye laser operating at 585 nm with pulse width of 0.5 μs, repetition rate of 19 s^{-1}, and an average output power of 0.13 watt. Doubling in an ADA crystal produces the 293 nm UV beam which is then circularly polarized and directed into the Tl cell containing Tl vapor at $T = 1050$ K and density $\sim 10^{15}$ atoms/cm^3. Tantalum electrodes inside the cell generate E_s which is set at 300 volt/cm to boost the fluorescence above background. After the main cell, the UV beam enters a second Tl vapor cell where the fluorescence is used to set L1 to the desired hyperfine component of the line.

A second dye laser L2 is pumped synchronously with L1 and used to drive an optical parametric oscillator (OPO) laser tuned to 2.18 μm. The IR output is circularly polarized and directed through interaction region 1 of the main cell and then reflected back with opposite J_z through a similar region 2. The fluorescence signal $(I_1 - I_2)/(I_1 + I_2)$ is proportional to P_z while strongly rejecting intensity variations. Let Δ be the observed part of Δ_{12} that is odd under both E_s and η_{IR} reversal. Under η_{UV} reversal, Δ should have an even part Δ^M that measures $\mathcal{M}$ and an odd part Δ^{PNC} that measures $\mathcal{E}_{PNC}$.

In an early experiment data was taken on the two hyperfine components $(F \to F')$ $0 \to 0$ and $0 \to 1$ separated by about 2 GHz. Calculation of P_z showed that the $0 \to 1$ transition has PNC and M1 contributions Δ_{01}^{M} and Δ_{01}^{PNC}, whereas for the $0 \to 0$ transition, $\Delta_{00}^{M} = \Delta_{00}^{PNC} = 0$. The procedure for taking data was to switch the UV laser wavelength from one hyperfine transition to the other approximately every 20 minutes. The observed values of Δ_{01}^{PNC} and Δ_{00}^{PNC} were found to vary systematically over periods of hours, but to be correlated such that $\Delta_D^{PNC} \equiv \Delta_{01}^{PNC} - \Delta_{00}^{PNC}$ appeared to have only a random statistical variation. The result of the initial 200 hours of data, quoted in terms of a circular dichroism δ

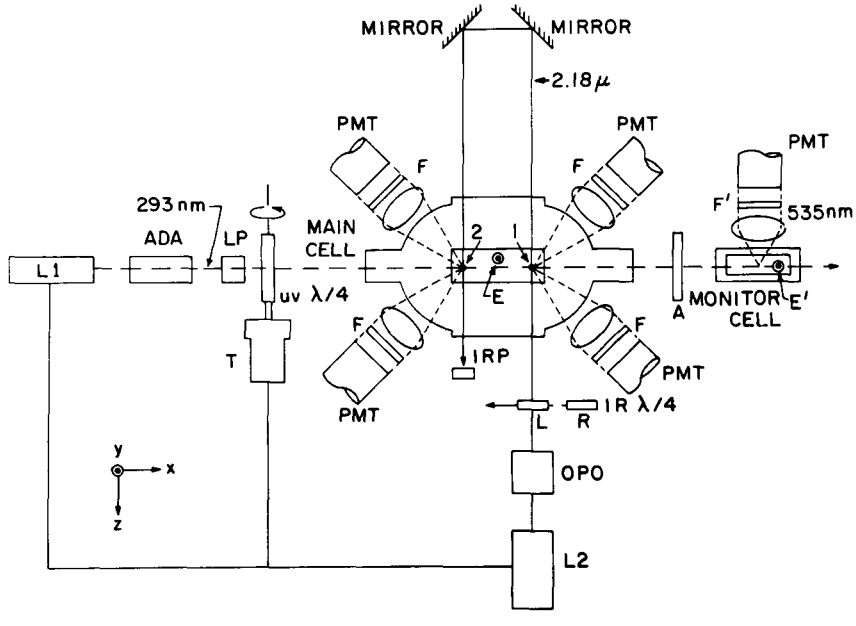

Fig. 13. Block diagram of the Berkeley thallium experiment.

defined in eq. (10), was $\delta_{exp} = +(5.2 \pm 2.4) \times 10^{-3}$ [75]. This can be compared with the theoretical values calculated from eqs. (45) and (46):

$$\delta_{theo} = +(1.8 \pm 0.2) \times 10^{-3} \tag{58}$$

for $\sin^2 \theta_w = 0.23$, reduced by radiative corrections [25, 34]. The calculation leading to eq. (58) has been outlined in section 5.2.1. The uncertainty in δ_{theo} comes from estimated uncertainties in $\mathcal{M}_{exp}$ (15%) [18]. Although quoting the result in terms of δ is convenient, it should be borne in mind that the observed fractional effect $\Delta^{PNC} \sim 10^{-5}$ is much smaller than δ.

After the above preliminary results were obtained, the Berkeley experiment was modified to include measurement of possible systematic errors due to strong electric fields (discussed in section 5.3 above) and to imperfect circular polarization. A number of measurements were taken with and without the UV beam reflected back through the cell. Systematic shifts were determined in auxiliary measurements [76] and subtracted from the observed asymmetry to arrive at the true PNC asymmetry. The details of this procedure have been published [76]. The result of this experiment yielded the PNC circular dichroism for Tl [76]:

$$\delta_{exp} = 2.8^{+1.0}_{-0.9} \times 10^{-3} . \tag{59a}$$

Comparison with eq. (58) shows the experimental and theoretical values overlap within their uncertainties.

More recently, an improved Tl measurement has been carried out at Berkeley utilizing a crossed magnetic field to measure the pseudoscalar, $\boldsymbol{B} \cdot \eta \boldsymbol{K} \times \hat{\boldsymbol{E}}_s$, a method also being pursued elsewhere with Cs as mentioned in section 5.3. A new result has been obtained which agrees with eq. (59a) above, with only about one-half the uncertainty quoted there [77]. They now give a result in terms of

$$\mathrm{Im}\ \mathscr{E}_{PNC}/\beta = -1.73 \pm 0.33\ \mathrm{mV/cm} \tag{59b}$$

which corresponds to a circular dichroism of

$$\delta_{exp} = (2.70 \pm 0.5) \times 10^{-3} \tag{59c}$$

where most of the uncertainty is statistical.

6. Atomic hydrogen experiments

PNC measurements in hydrogen and deuterium are of great fundamental interest. The most exciting prospect, if the experiments can achieve sufficient accuracy, is the possibility of testing the second-order predictions [25] of the Weinberg–Salam theory. These effects involve the exchange of two bosons (i.e. two Z_0, two $W^{\pm}$, or a Z_0 and a photon), and are analogous to the radiative corrections of quantum electrodynamics. They go to the heart of any gauge theory. The loop diagrams that contribute at this level involve momentum transfers of order 100 GeV/c. Short of this goal, H and D measurements still offer the important opportunity of determining all four neutral-current coupling constants of eq. (19). The atomic theory in H and D is of course totally reliable.

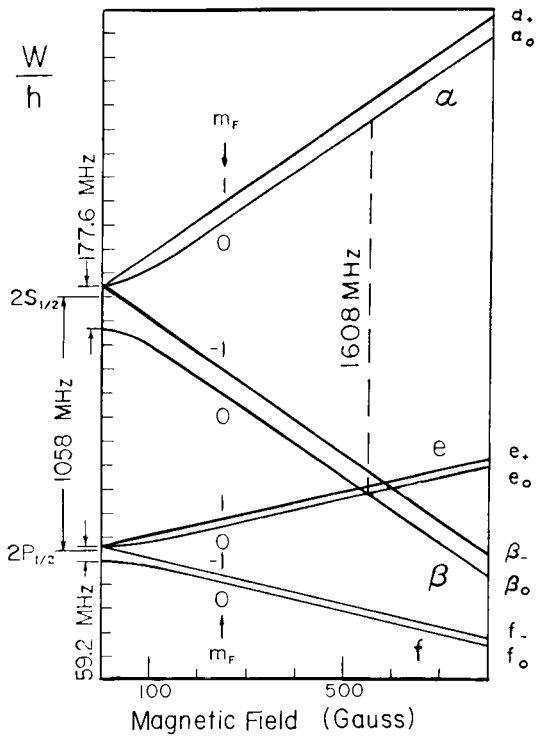

Fig. 14. Magnetic field dependence of atomic hydrogen energy levels.

Although there were earlier proposals for measuring PNC in hydrogen, the present interest began with studies by Lewis and Williams [19]. Later, attention at many laboratories started to focus on radio-frequency transitions among sublevels of the $2S_{1/2}$ state, and led to several experiments now underway [19, 21], although no results precise enough to test the theory are yet available from any hydrogen experiments.

The hydrogen experiments are made possible by the proximity of the opposite parity levels 2S and 2P. In fig. 14 we show the energies of the $2S_{1/2}$ and $2P_{1/2}$ magnetic sublevels in hydrogen as a function of external magnetic field. H_{PNC} connects opposite parity levels of the same angular momentum, such as β_0 with e_0 and f_0, or β_- with f_-. The crossing near 0.057 T (570 gauss) emphasizes β_0–e_0 mixing which is sensitive only to nucleon axial vector coupling (the C_2 terms in eqs. (21) and (24)), while the β–f crossings near 1150 G are sensitive to both electron and nucleon axial couplings (both C_1 and C_2 terms).

A complete tabulation of all the relevant matrix elements appears in Dunford et al. [21]. Here we will give only the β_0–e_0 mixing:

$$V_{\mathrm{PNC}} \equiv \langle \beta_0 | \frac{H_{\mathrm{PNC}}}{\hbar} | e_0 \rangle = -0.026 C_2 \quad (\text{in Hz}) . \tag{60}$$

One place to look for the weak interaction radiative corrections mentioned above is the β_0–e_0 crossing in deuterium, because the lowest order Weinberg–Salam theory predicts $C_{2\mathrm{p}} + C_{2\mathrm{n}} = 0$ as seen in eq. (19). The second-order W-S prediction for $C_{2\mathrm{p}} + C_{2\mathrm{n}}$ does not vanish, but gives a radiative correction of order 0.02 [24]. A competing effect induced by the weak nucleon–nucleon PNC interaction appears to be smaller [78] but may still cause some uncertainty. Careful measurements of both $C_{2\mathrm{p}}$ and

C_{1p} in hydrogen would be free of known competing effects and would allow accurate determination of both $\sin^2\theta_w$ and the second-order effects. Note that the accepted value of $\sin^2\theta_w$ (eq. (18)) makes the first-order values of C_{1p} and C_{2p} by eq. (19) turn out to be quite small, of order 0.04 and comparable to the second-order predictions.

Each experiment now underway in hydrogen employs a different scheme for observing PNC interference. For definiteness, we will concentrate here on the University of Washington experiment which in its first stage is designed to detect Stark-PNC interference in the $\alpha_0 \rightarrow \beta_0$ transition in a magnetic field set near the β–e crossing of fig. 14. Two RF cavities are used, as shown in fig. 15. The Stark amplitude

$$A_s(\alpha_0 \xrightarrow{R^I} e_0 \xrightarrow{V_s} \beta_0)$$

produced in cavity I interferes with the PNC amplitude

$$A_{PNC}(\alpha_0 \xrightarrow{R^{II}} e_0 \xrightarrow{V_{PNC}} \beta_0)$$

produced in cavity II. In each cavity there is a radio-frequency field $E_{RF}\,e^{i\omega t}$ parallel to $\hat{z}$, the direction of the static magnetic field $\boldsymbol{B}$, and oscillating near the $\alpha_0 \rightarrow e_0$ transition frequency at $\omega \cong 2\pi \times 1608\,\text{MHz}$. We define:

$$R^{I,II} \equiv E^{I,II}_{RF}\langle e|\hat{z}\cdot\boldsymbol{E}1|\alpha_0\rangle/2\hbar\,. \tag{61}$$

In cavity I there is also a static electric field E_0 parallel to $\hat{z}$ which Stark mixes the β_0 and e_0 states with a matrix element:

$$V_s \equiv E_0\langle\beta_0|\hat{z}\cdot\boldsymbol{E}1|e_0\rangle/\hbar\,. \tag{62}$$

This matrix element is reduced by about a factor of 20 below the full E1 strength because the e_0 and β_0 states have nearly opposite nuclear spin directions at 0.057 T.

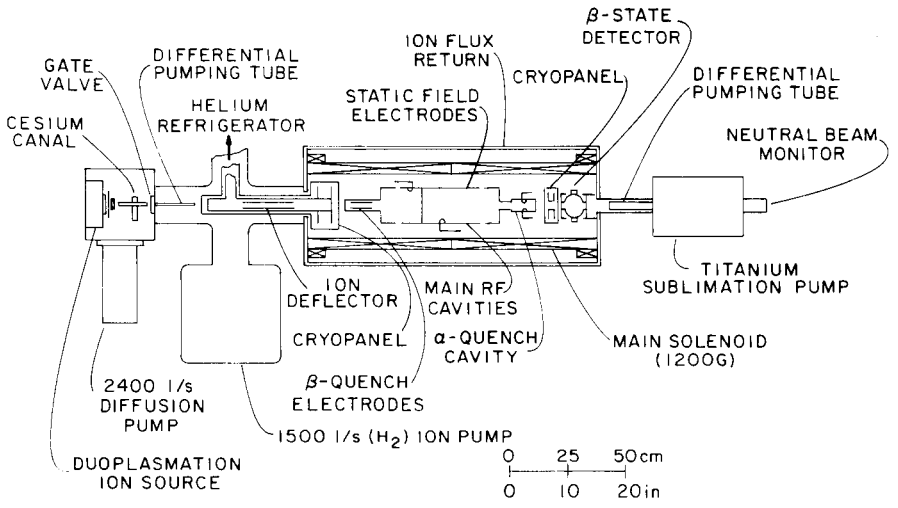

Fig. 15. Block diagram of the Seattle hydrogen experiment.

Assuming V_x and V_{PNC} are small enough for first-order perturbation theory, we may use eqs. (1) and (13) together with (61) and (62) above to obtain:

$$\begin{aligned} \boldsymbol{E}^{\mathrm{I}}_{\mathrm{RF}} \cdot \boldsymbol{\mathscr{E}}_{\mathrm{s}} &\equiv \boldsymbol{E}^{\mathrm{I}}_{\mathrm{RF}} \cdot \langle \beta_{\mathrm{s}} | \boldsymbol{E}1 | \alpha_{\mathrm{s}} \rangle \cong \frac{R^{\mathrm{I}} V_{\mathrm{s}}}{(E_{e_0} - E_{\beta_0})/\hbar + \mathrm{i}\gamma/2} \\ \boldsymbol{E}^{\mathrm{II}}_{\mathrm{RF}} \cdot \boldsymbol{\mathscr{E}}_{\mathrm{PNC}} &\equiv \boldsymbol{E}^{\mathrm{II}}_{\mathrm{RF}} \cdot \langle \beta_{\mathrm{PNC}} | \boldsymbol{E}1 | \alpha_{\mathrm{PNC}} \rangle \cong \frac{R^{\mathrm{II}} V_{\mathrm{PNC}}}{(E_{e_0} - E_{\beta_0})/\hbar + \mathrm{i}\gamma/2} \end{aligned} \tag{63}$$

where we have added to the energy denominators the decay rate γ of the $2P_{1/2}$ state, omitted previously because the energy separations were much larger than $\hbar\gamma$ in all the heavy atom experiments. Here, $\gamma/2\pi \cong 100$ MHz.

If the atoms spend times t_{I} and t_{II} in the two cavities, and if $R^{\mathrm{I}}t_{\mathrm{I}}$ and $R^{\mathrm{II}}t_{\mathrm{II}}$ are both small ($\ll 1$), then we may write:

$$\begin{aligned} A_{\mathrm{PNC}} &\cong \frac{R^{\mathrm{II}} V_{\mathrm{s}} t_{\mathrm{II}}}{(E_{e_0} - E_{\beta_0})/\hbar + \mathrm{i}\gamma/2} \\ A_{\mathrm{S}} &\cong \frac{R^{\mathrm{I}} V_{\mathrm{PNC}} t_{\mathrm{I}}}{(E_{e_0} - E_{\beta_0})/\hbar + \mathrm{i}\gamma/2} . \end{aligned} \tag{64}$$

The assumption that $R^{\mathrm{II}}t_{\mathrm{II}} \ll 1$ is not true in practice. (In fact, as we will see later, optimally $R^{\mathrm{II}}t_{\mathrm{II}} \cong \sqrt{\gamma/t_{\mathrm{II}}}$.) Thus eq. (64) gives only a rough value of the amplitudes. In the case of arbitrary strengths of applied fields, the correct equations are discussed in ref. [20].

The total transition probability for the usual situation when $|A_{\mathrm{PNC}}| \ll |A_{\mathrm{S}}|$ is:

$$|A_{\mathrm{PNC}} + A_{\mathrm{S}}|^2 \cong |A_{\mathrm{S}}|^2 + 2\,\mathrm{Re}[A_{\mathrm{PNC}} A_{\mathrm{S}}] \tag{65}$$

where the second term gives the Stark-PNC interference and is maximum when A_{PNC} and A_{S} have the same phase. Since by eq. (4) V_{PNC} is pure-imaginary, while V_{s} is real, it is necessary to maintain a phase difference of $\pi/2$ between R^{I} and R^{II} by adjusting the relative phase of the RF fields in the two cavities. In practice this important adjustment is made by applying a small Stark field in cavity II and setting the RF phase in cavity I, $\phi^{\mathrm{I}}_{\mathrm{RF}}$, such that the interference between $A^{\mathrm{I}}_{\mathrm{S}}$ and $A^{\mathrm{II}}_{\mathrm{S}}$ vanishes.

The handedness of the PNC effect should be revealed in the T even pseudoscalar $(\boldsymbol{E}^{\mathrm{II}}_{\mathrm{RF}} \cdot \boldsymbol{E}^{\mathrm{I}}_{\mathrm{RF}})\boldsymbol{E}^{\mathrm{I}}_{\mathrm{S}} \cdot \boldsymbol{B}$ and the interference term in eq. (65) will reverse sign when $\boldsymbol{B}$ or $\boldsymbol{E}_{\mathrm{S}}$ is reversed, or when $\phi^{\mathrm{I}}_{\mathrm{RF}}$ is changed by π.

Clearly, increasing R^{II} increases the fractional size of A_{PNC} in eq. (65). However R^{II} also causes $\alpha_0 \rightarrow e_0$ transitions, and an upper limit to the useful size of R^{II} is set by the radiative decay it induces in α_0 via the e_0 state,

$$R^{\mathrm{II}\,2}_{\mathrm{max}} \cong [\gamma^2 + |(E_{e_0} - E_{\beta_0})/\hbar^2|^2]/\gamma t . \tag{66}$$

Far off resonance, $R^{\mathrm{I}}_{\mathrm{max}}$ increases with the energy difference $|E_e - E_\beta|$ in such a way as to compensate A_{PNC} in eq. (65), so that the fractional size of PNC interference actually obtainable is rather independent of the magnetic field in fig. 14, provided R^{II} can be made large enough. A measurement at zero magnetic field can be of comparable sensitivity as at the level crossings, and offers the advantage of eliminating any spurious effects due to electric fields $\boldsymbol{E}_{\mathrm{m}} = \boldsymbol{v}/c_{\mathrm{l}} \times \boldsymbol{B}$ arising from motion of the atoms not

exactly parallel to the magnetic field. An experiment is presently underway that uses the hfs transitions near zero B [79].

The apparatus used in the University of Washington hydrogen experiment is shown in fig. 15. Protons from a duo-plasmatron, converted by charge exchange in Cs vapor into a beam of H(2S), enter a 0.057 T solenoid. The beam passes through a static electric field to quench the β levels. The resulting beam of atoms in the α_0 and α_+ states then enters two successive cavities oscillating coherently near 1608 MHz. These are the cavities producing separately the Stark and PNC transition amplitudes from α_0 to β_0 as discussed above. The PNC cavity is about 50 cm long. This cavity also has a static electric field along $\hat{z}$ to drive a useful probe transition for adjusting the relative phases of the two cavities. The beam then passes through another rf cavity oscillating at 2143 MHz which removes any population remaining in the α_+ and α_0 levels by α–f mixing. The β states produced in the Stark and PNC cavities are then detected when the beam passes through a static electric field that quenches them via the e state, producing Lyman α radiation. This radiation is the signal. Metastable beam intensities of 3×10^{13} particles/second through the apparatus have been obtained. Background counting rates with the beam turned on but the Stark and PNC cavities turned off are $<10^7$ particles/second. The expected fractional PNC interference is $\sim 10^{-6} C_{2p}$ when the Stark transition amplitude is adjusted to match background, i.e., to yield a counting rate at the detector of about 3×10^7 particles/second. About three hours of integration time would be required to resolve $C_{2p} = 1$.

Possibilities of developing slower metastable beams of comparable intensity, perhaps at thermal energies well below room temperature, are being explored; and some progress has been reported [80]. The overall sensitivity varies as the square-root of the flight time through the PNC cavity (see eq. (64) and the discussion below it), and thus improves with reduced beam speed. Motional electric fields are also reduced. A major limiting factor in all experiments will be the extent to which systematic effects from stray electric fields along the metastable beam can be reduced.

7. Experiments to find T-violating interactions (permanent EDM's)

In section 2 we pointed out that a PNC interaction that violates time-reveral symmetry can give rise to a permanent electric dipole moment (EDM) in an atom, and an energy shift of an atom in an external electric field. We have not had occasion to consider this point further because all the PNC effects thus far discussed possess time-reversal symmetry. We will now present a rather brief treatment of possible T-violation in atoms and the interpretation to be placed on past and future experimental searches for an atomic or molecular EDM.

The motivation for an EDM search is the long standing observation of CP violation in K_0 decay [29] which, coupled with the TCP theorem, requires the existence of T-violation as well. An argument also has been given [81] that the K_0 experiments show T-violation directly, without recourse to the TCP theorem. Unfortunately there is no successful theory akin to the Weinberg–Salam–Glashow electro-weak theory to guide us in the choice of a single T-violating interaction in atoms. Some fundamental mechanisms that have been proposed as a source of T-violation are listed at the beginning of section 7.2 below. These theories lead to many possible interactions in atoms, three of which we will consider. One is a short-range T-violating PNC force between electrons and nucleons, the second is an interaction of atomic electrons with an EDM charge distribution in the nucleus, and the third is the effect on an atom of an intrinsic EDM of the electron. Other important possibilities which we will not discuss here include the effect of higher T-odd multipole moments in the nucleus [7, 82, 83].

7.1. *T-violating short-range PNC force between electrons and nucleons*

The most general nonderivative short-range neutral current interaction that violates both parity conservation and time-reversal symmetry is automatically restricted to Lorentz scalar and tensor terms, and may be written:

$$H_{\mathrm{PNC}} = \mathrm{i}C_{\mathrm{s}}\frac{G_{\mathrm{F}}}{\sqrt{2}}\sum_{n,e}(\bar{n}n)(\bar{e}\gamma_5 e) + \mathrm{i}C_{\mathrm{t}}\frac{G_{\mathrm{F}}}{\sqrt{2}}\sum_{n,e}(\bar{n}\gamma_5\sigma_{\mu\nu}n)(\bar{e}\sigma^{\mu\nu}e)\,, \tag{67}$$

where $\sigma_{\mu\nu} = \frac{1}{2}(\gamma_\mu\gamma_\nu - \gamma_\nu\gamma_\mu)$, and the dimensionless constants C_{s} and C_{t} measure the magnitudes of the scalar and tensor interactions. We have left out any isospin dependence in the nucleon current, and have let n and e stand for the nucleon and electron wave functions.

Using the usual approximations (relativistic electrons, nonrelativistic nucleons; see eq. (20)) one can readily show that the scalar term depends mainly on the electronic angular momentum $\boldsymbol{J}$ whereas the tensor term depends mainly on the nuclear spin $\boldsymbol{I}$. Thus the EDM energy shift given by eq. (5) may be written in the form

$$\delta E = \mathscr{E}_{\mathrm{s}}\frac{\boldsymbol{J}}{J}\cdot\boldsymbol{E} + \mathscr{E}_{\mathrm{t}}\frac{\boldsymbol{I}}{I}\cdot\boldsymbol{E}\,. \tag{68}$$

We can estimate the sizes of $\mathscr{E}_{\mathrm{s}}$ and $\mathscr{E}_{\mathrm{t}}$, and also bring out some features of this T-violating interaction, by writing the interaction in the completely nonrelativistic limit for both electrons and nucleons. For example, in this limit the scalar terms of the interaction become

$$(H_{\mathrm{PNC}})_{\mathrm{s}} = C_{\mathrm{s}}\frac{\mathrm{i}G_{\mathrm{F}}}{2\sqrt{2}}\frac{\boldsymbol{p}\cdot\boldsymbol{\sigma}}{m_e c}\,\delta(\boldsymbol{r}) + \text{Hermitian conjugate} \tag{69}$$

which, except for the all-important factor of i, is identical to the $C_{1\mathrm{N}}$ terms of the T-symmetric interaction shown earlier in eq. (24). Since, as we have already seen, the interaction in eq. (24) leads to a purely imaginary $\mathscr{E}_{\mathrm{PNC}}$, it is clear that the above factor of i leads to a purely real $\mathscr{E}_{\mathrm{s,t}}$ as expected for a T-violating H_{PNC}.

Just as in the T-symmetric case, the PNC effects here also rise rapidly with increasing atomic number Z. Using eqs. (25), (26) and (69), we arrive at the analog of eq. (27), this time for the T-violating case:

$$\begin{aligned}\mathscr{E}_{\mathrm{s}} &\cong 10^{-16}Z^2 Q_{\mathrm{s}} K_{\mathrm{r}} C_{\mathrm{s}}(ea_0)\\ \mathscr{E}_{\mathrm{t}} &\cong 10^{-16}Z^2 K_{\mathrm{r}} C_{\mathrm{t}}(ea_0)\,,\end{aligned} \tag{70}$$

where K_{r} again is a relativistic factor that increases with Z, becoming about 3 for Cs and about 9 for Hg or Tl. Q_{s} is a factor of order Z that depends upon the isospin structure of the interaction, and is the analog of Q in eq. (23). The nuclear spin term ($\mathscr{E}_{\mathrm{t}}$) is missing this enhancement factor.

Accurate atomic calculations start with eq. (67) and use fully relativistic electron wave functions in the case of heavy atoms. Such calculations have been carried out for a number of atoms. We quote here

some results for ^{133}Cs [84], metastable ^{129}Xe [85], and ^{199}Hg [86]:

$$\begin{aligned}
&\mathscr{E}_s(^{133}\mathrm{Cs}) = 1.3\times 10^{-12} Q_s e a_0 C_s \\
&\mathscr{E}_s(^{129}\mathrm{Xe}) = 1.8\times 10^{-12} Q_s e a_0 C_s\,; \qquad (5p^5 6s \text{ state}) \\
&\mathscr{E}_t(^{199}\mathrm{Hg}) = 1.5\times 10^{-11} e a_0 C_t\,.
\end{aligned} \tag{71}$$

In a practical experiment the atom is placed in parallel magnetic and electric fields and the Zeeman precession frequency ν_Z of the spins in the magnetic field is measured. When the electric field direction is reversed, the energy shift in eq. (5) causes a shift $\delta\nu_Z$ of magnitude $2\mathscr{E}_s E/Jh$ (or $2\mathscr{E}_t E/Ih$). In the case of Hg, for example, one obtains

$$\delta\nu_Z(^{199}\mathrm{Hg}) = 0.1 C_t E \qquad (E \text{ in kV/cm}, \delta\nu_Z \text{ in Hz})\,. \tag{72}$$

Sandars [87] has pointed out an important EDM enhancement in polar molecules that applies to the effect of the short-range T-violating force under discussion here, and also to the effect of an EDM in the nucleus to be discussed below. In a readily attainable laboratory electric field, a polar molecule such as TlF can be strongly polarized with its polar axis along the field. In this case, the very large internal molecular electric field causes a large mixing of electronic states having opposite parity in a frame centered on the Tl (or F) nucleus, which then couples to the nucleon spin component along the polar axis through eq. (67). An alternative and equivalent picture is that the internal T-violating interaction induces an electronic polarization that ultimately couples together opposite parity rotational states of the molecule, which in TlF, for example, are separated by only $\cong 10^{-4}$ eV compared with several eV characteristic of opposite parity state separations in atoms. TlF is a good polar molecule to choose because the Tl nucleus contributes with the $K_r Z^2$ enhancement factor of eq. (70). A calculation using the interaction in eq. (67) with TlF yields the value [85]:

$$\delta\nu_Z(\mathrm{Tl\ in\ TlF}) = 2.8\times 10^3 C_t \text{ (in Hz)} \tag{73}$$

for the shift in the Zeeman frequency of the Tl nucleus under reversal of a 50 kV/cm laboratory field applied to the molecule. Such calculations in molecules are difficult, and the above number must be considered to have a large uncertainty [26] until more complete calculations are carried out. By comparing eq. (72) with eq. (73), it is apparent that the EDM shift in a heavy molecule is more than 100 times larger than it is in a heavy atom in the same external electric field. On the other hand, atoms such as Xe and Hg can have much sharper Zeeman resonance lines [28, 88] than polar molecules, with possibly a larger signal size as well, allowing smaller shifts to be measured in the case of such atoms. On balance, it is difficult to tell in advance which system ultimately can be made the most sensitive to EDM effects, and it is best to pursue all reasonable alternatives.

Atomic and molecular experiments have set limits on both C_s and C_t in eq. (67). Experimental limits on $\mathscr{E}_S$ in cesium [89] and in metastable xenon [90], each having an unbalanced electron spin, in conjunction with calculations (see eq. (71)) have set a limit of:

$$C_s \leq 2\times 10^{-4}(Q_s/100) \tag{74}$$

where a reasonable assumption would be $Q_s \cong 100$. Experimental limits [26] on $\mathscr{E}_T$ in TlF taken

together with the theoretical result in eq. (73) may be interpreted as setting a comparable limit on C_t. Experiments on Xe atoms [28] recently have set a more precise limit, $C_t < 10^{-6}$, and have set the most precise EDM limit on any atomic or nuclear system, $d(^{129}\text{Xe}) < 10^{-26}$ e-cm [88].

7.2. Atomic effects of an EDM distribution in the nucleus

An electric dipole distribution of charge in the nucleus could arise by any of the mechanisms that have been proposed as a potential source of an EDM of the neutron, currently known to be $<3\times 10^{-25}$ e-cm [6]. These mechanisms include the original "super-weak" proposal [91], T-violation at a quark–boson weak interaction vertex (the Kobayashi–Moskawa model [92]), T-violation in the "Higgs-sector" of gauge theories [93], left–right symmetric theories [94], and T-violation associated with the vacuum parameter θ_{QCD} [95] in grand unified theories, including a possible cosmologically determined lower limit on a neutron EDM [96]. We will not go into these interesting theories here, except to note that any of them could lead to a quark–quark or nucleon–nucleon PNC interaction that would be T-odd, and therefore could induce a dipole distribution of charge in the nucleus much as eq. (5) leads to a dipole distribution of charge in an atom. Work has begun [97] on calculating the size of the EDM in nuclei based on some of these theories.

The size of the EDM produced in a nucleus by interaction among the nucleons might well be larger than the EDM in a single nucleon, by virtue of the higher polarizability of the nucleus. However, as we will see shortly there is always a large reduction of the EDM in the atoms as a whole because of shielding. The net result is that there is some promise in searching for nuclear EDM effects in polar molecules and in certain heavy atom gases and vapors with long nuclear spin relaxation times – the same favorable cases already described in section 7.1.

An important consideration first discussed in detail by Schiff [98] is the shielding of an externally applied electric field by the atomic electrons so as to reduce the net electric force on the nucleus to zero. Otherwise, the charged nucleus would not be in equilibrium. In fact, Schiff proved that an EDM on any charged particle in a neutral system that is in equilibrium under only electrostatic forces can produce no net energy shift when an electric field is applied to the system.

If some other force, such as a magnetic interaction, also couples to the nucleus, then some fraction of an external field can still exist at the nucleus, allowing an energy shift by a nuclear EDM. Also, the distribution of nuclear charge and of electric dipole moment need not coincide, leading to a net electric field averaged over the EDM distribution in the nucleus when the field averaged over the charge distribution is zero. These two effects are called respectively, the magnetic effect and the volume effect. The magnetic effect dominates in light atoms and contributes to the atomic EDM in hydrogen an approximate size of

$$(\text{EDM})_{\text{atom}} \cong 2\frac{m}{M}(\text{EDM})_{\text{proton}} \tag{75}$$

where m and M are the electron and proton masses. This effect rises roughly as the atomic number Z as we go to heavy atoms. The volume effect dominates in heavy neutral atoms, and contributes an order of magnitude value:

$$(\text{EDM})_{\text{atom}} \cong K_r Z^2 (r_N/a_0)^2 (\text{EDM})_{\text{nucleus}}, \tag{76}$$

where r_N is the nuclear radius, a_0 the Bohr radius, and K_r the relativistic factor discussed with eq. (70).

The enhancement with increasing Z results because only the electronic wave function within the nuclear volume contributes to the effect [26], and thus the Z dependence of the s and p wave functions near the origin, as shown earlier in eqs. (25) and (26), is important.

Similar considerations apply to estimating the effect of an intrinsic EDM of an individual nucleon in the nucleus. This case in fact is the one for which systematic calculations have been carried out so far. The induced dipole moments of the Tl atom and of the TlF molecule have been calculated when the odd proton in the thallium nucleus is assumed to have an EDM. For the volume effect, which dominates over the magnetic effect in Tl, the results are [7, 26]:

$$\begin{aligned}(\mathrm{EDM})_{\mathrm{Tl}} &= 0.001\,(\mathrm{EDM})_{\mathrm{proton}} \\ (\mathrm{EDM})_{\mathrm{TlF}} &= 0.2\,(\mathrm{EDM})_{\mathrm{proton}} \qquad [50\ \mathrm{kV/cm\ applied}]\,,\end{aligned} \tag{77}$$

where the enhancement in the polar molecule is again comparable to that discussed in section 7.1. This theoretical result has been combined with the experimental $(\mathrm{EDM})_{\mathrm{TlF}}$ limit (also discussed in section 7.1) to yield an upper limit on the proton EDM at the level of 10^{-21} e-cm [26]. Presumably, a comparable limit would apply to an EDM charge distribution in the nucleus due to nucleon–nucleon P and T violating forces, although the nuclear structure details have not been worked out. Continued experimental work on TlF, and the recently begun experiments on Hg and Xe [28, 88] and on ^{19}Ne [99] may well yield improved sensitivity to a nuclear EDM by several orders of magnitude.

7.3. Atomic effects of an intrinsic EDM of the electron

The mechanisms mentioned at the beginning of section 7.2 whereby a nucleon might acquire an EDM would, when applied to an electron, produce an undetectably small dipole moment. However, as emphasized by many authors [100] recently, the origin of CP or T violation remains completely uncertain, and one can readily construct theories in which the intrinsic EDM of an electron would be comparable to that of a neutron.

A remarkable feature of heavy atoms with unbalanced electron spin is that the effect of the electron EDM gets multiplied by a large factor, producing a much greater dipole moment of the entire atom. This enhancement was first discovered by Sandars [101]. It amounts to a factor of order 100 in the important cases of Cs and metastable Xe. This was the first example found of the large growth of parity violating effects with increasing Z.

The enhancement in heavy atoms is all the more striking in view of the large *reduction* of the effect of the electron EDM in a light atom such as hydrogen. The origin of the rapid increase of the induced atomic EDM with atomic number Z is closely related to the similar increase in atomic dipole moment in all the cases considered in this article (eqs. (27), (70) and (76)). Once again, it turns out that the atomic moment rises as Z^3.

To understand the electron EDM enhancement, first recall the argument of the previous section that, in the absence of non-electrostatic forces, an external electric field produces zero net field on a charged particle inside a neutral atom. There is a non-electrostatic force, however; it is the spin–orbit interaction in the atom, which provides a magnetic force to balance a net electric force on the electron. The net electric field that an electron "sees" is clearly very small in a light atom, of order α^2 times the applied field in the case of hydrogen, i.e. the same order as the spin–orbit interaction. However, as we go to heavy neutral atoms, it is well known that the spin–orbit interaction varies roughly as $Z^2\alpha^2$. This increase with Z^2 is almost entirely due to the behavior of the interaction rather close to the nucleus in

the unshielded part of the nuclear Coulomb field where there is a large $\boldsymbol{v} \times \boldsymbol{E}$ magnetic field and a larger electron probability density as described in eq. (25).

A third factor of Z appears in the EDM effect because the coupling of the dipole with the Coulomb field $eZ_{\rm eff}/r^2$, and the electron probability density at the origin combine to make the dominant contribution fall inside the first node of the radial wave function where $Z_{\rm eff} \sim Z$. The net result is that the atom acquires a dipole moment of approximate magnitude:

$$(\mathrm{EDM})_{\rm atom} \cong \alpha^2 Z^3 K_{\rm r} (\mathrm{EDM})_{\rm electron} \tag{78}$$

where $K_{\rm r}$ is the relativistic enhancement used in eq. (70). In some atoms, such as Cs, the high polarizability contributes a further enhancement to eq. (78).

Accurate calculations by Sandars [7, 101] have been applied to the experimental limits on atomic EDMs in Cs [89] and metastable Xe [90] to yield an upper limit on an intrinsic electron dipole moment:

$$(\mathrm{EDM})_{\rm electron} \leqq 2 \times 10^{-24}\ \text{e-cm}\,. \tag{79}$$

It is possible that a new program of optical pumping experiments [28] when applied to Cs atoms [102], will yield improvements in the above limit and in the limit on $C_{\rm s}$ given in eq. (74).

In an atom with $^1S_0$ electronic structure, an electron EDM can induce an overall atomic EDM parallel to the nuclear spin, because of the hyperfine coupling between the electronic and nuclear spins [103]. Thus experiments with ground state Xe or Hg [28], because of their great sensitivity, may set a useful limit on an intrinsic electronic dipole moment.

8. Discussion of results; conclusions

After the digression in section 7 we return now to the observation of parity nonconservation in atoms, and discuss the experimental and theoretical results described in the earlier sections of this review.

As we have seen there now exist significant measurements of PNC in 4 different atoms, carried out on 5 distinct magnetic-dipole absorption lines. In table 5 we show the most recent result of each experiment together with the value predicted by the Glashow–Weinberg–Salam weak interaction theory. The predicted values are those we have reported in earlier sections based on described atomic calculations. We also show the values of Q and $\sin^2\theta_{\rm w}$, defined in eq. (17) and eq. (23), which may be inferred in each case from the experimental result and the atomic calculations.

In general, these results demonstrate that parity conservation is violated in atoms at the level predicted by the Weinberg–Salam theory. To discuss the collection of atomic results quantitatively, we treat the error in measuring Q (and $\sin^2\theta_{\rm w}$) on each absorption line as independent of the errors associated with the other absorption lines. The different experiments should clearly have uncorrelated uncertainties, but the atomic calculations of the two Bi lines and to some extent of the Pb line could in principle have common errors. However, even between the two bismuth lines there are significant differences in those portions of the atomic calculations that involve the major uncertainties, namely in the noncentral electron–electron interactions. As it turns out, the final number is not much affected by whether we take the bismuth results as independent or not. With some justification therefore, we simply take an average of the values in table 5 and obtain the mean value

$$Q^{\rm meas}/Q^{\rm w-s} = 1.00 \pm 0.17 \tag{80}$$

(using $\sin^2\theta_{\rm w} = 0.23$ and making radiative corrections [25, 34]).

Table 5
Comparison of predicted and measured results of the atomic experiments

Transition (nm)	Experimental quantity	Experimental value	Theoretical value (a)	$\sin^2\theta_w$ (experimental) (b)	$\frac{Q^{exp}}{Q^{w-s}}$ (c)
Bi (876)	Im $\mathscr{E}_{PNC}/\mathscr{M}$	$(-10.5 \pm 1.3)\times 10^{-8}$ (f)	-10×10^{-8} (g)	0.23	1.05
Bi (648) (d)	Im $\mathscr{E}_{PNC}/\mathscr{M}$	$(-9 \pm 2)\times 10^{-8}$ (h)	-13×10^{-8} (g)	0.11	0.69
Pb (1279)	Im $\mathscr{E}_{PNC}/\mathscr{M}$	$(-9.9 \pm 2.5)\times 10^{-8}$ (i)	-13×10^{-8} (j)	0.13	0.76
Tl (293)	2 Im $\mathscr{E}_{PNC}/\mathscr{M}$	$(2.7 \pm 0.5)\times 10^{-3}$ (k)	1.8×10^{-3} (l)	0.38	1.55
Cs (539) (e)	Im$(\mathscr{E}_{PNC}/\beta)$	$-1.56 \pm 0.17 \pm (\sim 0.12)$ mV/cm (m)	-1.61 mV/cm (n)	0.20	0.97

Average $Q^{exp}/Q^{w-s} = 1.00 \pm 0.17$
Average $\sin^2\theta_w(\text{exp}) = 0.21 \pm 0.05$ (b)

(a) Theoretical values are averaged from those atomic calculations which include the major corrections to the central field independent particle model (IPM). The Weinberg–Salam theory is assumed, with $\sin^2\theta_w = 0.23$. An effective value of $\sin^2\theta_w$ ($\cong 0.21$) is picked for each element to take radiative corrections into account (see refs. [25] and [34]).

(b) An effective value using $Q = Z(1 - 4\sin^2\theta_w) - \eta$, not amended for radiative corrections. This value should be about 10% below the true value [25, 34].

(c) The ratio between the values in column 3 and column 4.

(d) For the 648 nm line we use the Oxford result which agrees with the average of the (mutually inconsistent) published results at 648 nm.

(e) The experimental value shows statistical and systematic errors in that order.

(f) Refs. [53, 47].
(g) Refs. [43, 44, 46].
(h) Ref. [56].
(i) Ref. [61].
(j) Ref. [46].
(k) Refs. [76, 77].
(l) Refs. [65, 66, 67]; $\mathscr{M}$ is the experimental value given in ref. [18].
(m) Refs. [71, 72] average of eqs. (55) and (56).
(n) Ref. [70].

Alternatively, the atomic experiments could be interpreted as measuring θ_w, yielding a mean effective value defined by $Q = Z(1 - 4\sin^2\theta_w) - \eta$:

$$(\sin^2\theta_w)_{\text{atoms}} = 0.21 \pm 0.05\,. \tag{81}$$

From this effective value one can infer a true value approximately 10% higher by taking radiative corrections into account [25, 34] as discussed below eq. (18), although in principle this must be done for each element separately before averaging. In both eqs. (80) and (81) the quoted uncertainty is one standard deviation on the data set.

In the above averages we use the Oxford experiment for the 648 nm line in bismuth. Taking an average of all 648 nm results would not alter the numbers significantly. The large discrepancy among the Novosibirsk, Moscow, and Oxford results, eqs. (41)–(43), is disappearing. The most recent results from Oxford and Moscow agree with each other and with the value we take in table 5. It should not be surprising that a few of several very challenging experimental measurements should lie outside the expected uncertainties. It is our opinion that the complete set of atomic measurements should be taken as rather forceful experimental affirmation of the standard model. It is clear that the Glashow–Weinberg–Salam theory, even with a generous uncertainty in θ_w, places a tight constraint on atomic PNC results which thus far is well satisfied within the experimental uncertainties.

If one adopts a model-independent approach to the weak neutral current interaction, the atomic experiments supply certain information about the coupling constants not provided by high energy

experiments. Combining all information sets stringent limits on the neutral current parameters, and thereby gives an exacting test of theories (including, but not restricted to the Weinberg–Salam model) that predict values of these parameters.

Using the simplest model-independent assumptions, Hung and Sakurai [104] characterize the theory by 10 coupling constants which must be determined by experiment. Of these all but four ($\tilde{\alpha}$, $\tilde{\beta}$, $\tilde{\lambda}$, $\tilde{\delta}$) are determined by neutrino experiments. These remaining four are defined in terms of the C parameters of eq. (19):

$$\begin{aligned} \tilde{\alpha} &\equiv \tfrac{1}{2}(C_{1p} - C_{1n}), \qquad \tilde{\gamma} \equiv \tfrac{1}{3}(C_{1p} + C_{1n}), \\ \tilde{\beta} &\equiv \tfrac{1}{2}(C_{2p} - C_{2n}), \qquad \tilde{\delta} \equiv \tfrac{1}{2}(C_{2p} + C_{2n}). \end{aligned} \tag{82}$$

The polarized electron scattering experiment [13] yields:

$$\begin{aligned} \tilde{\alpha} + \tfrac{1}{3}\tilde{\gamma} &= -0.60 \pm 0.16 \\ \tilde{\beta} + \tfrac{1}{3}\tilde{\delta} &= 0.31 \pm 0.51 . \end{aligned} \tag{83}$$

The heavy-atom experiments are sensitive to an almost orthogonal linear combination of $\tilde{\alpha}$ and $\tilde{\gamma}$:

$$Q(Z, N) = -(Z - N)\tilde{\alpha} - 3(Z + N)\tilde{\gamma} . \tag{84}$$

In fig. 16 we make a two-dimensional plot of $\tilde{\alpha}$ and $\tilde{\gamma}$, and show the area allowed by using eq. (84) and combining all atomic results from table 5. Once again, different measurements of Q are treated as independent in the sense discussed above eq. (80). Also shown in fig. 16 is the area allowed by the polarized electron scattering results (eq. (83)), plus further restrictions imposed on $\tilde{\alpha}$, $\tilde{\gamma}$ by neutrino experiments if the "factorization" hypothesis is included. One can see that the atomic PNC results

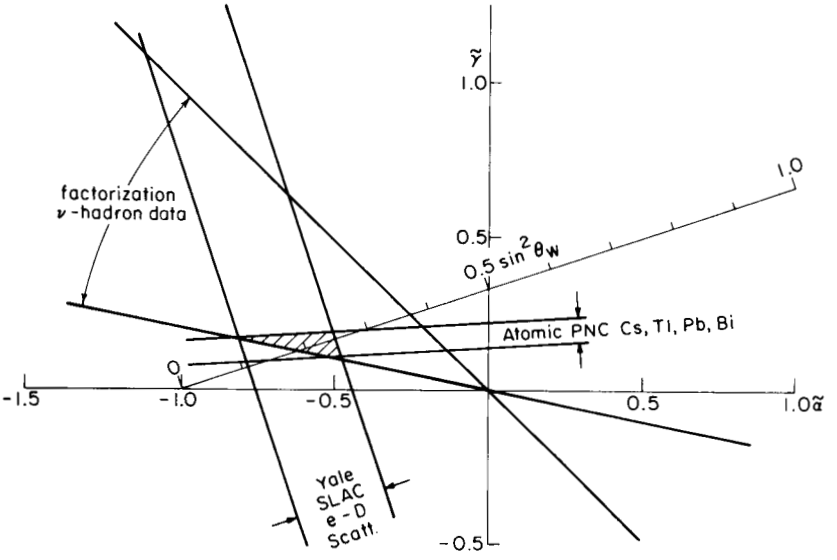

Fig. 16. Limits placed on coupling constants $\tilde{\alpha}$ and $\tilde{\gamma}$ by scattering experiments and atomic PNC experiments.

significantly exclude values of the parameters that would otherwise be allowed. It is noteworthy, of course, that the standard electro-weak theory falls within all allowed regions.

Using all data, the region allowed in the diagram yields:

$$\tilde{\alpha} = -0.68 \pm 0.15\,, \qquad \tilde{\beta} = 0.18 \pm 0.03\,. \tag{85}$$

Various theoretical models, other than Weinberg–Salam, can be tested against eq. (85). Here, for illustration, we will discuss one other class of models, namely those that include two or more neutral gauge bosons Z. As pointed out by Robinett and Rosner [23], atomic experiments set the most severe constraints on such models. For example, in the two-Z model considered by Robinett and Rosner the limits in eq. (85) imply that the mass of the two Z bosons must satisfy

$$\begin{aligned} &M_1 \cong M_0\,, \\ &M_2 \geqq 3M_0\,, \end{aligned} \qquad M_0 \cong 89\ \mathrm{GeV}\,, \tag{86}$$

the dominant restrictions coming from the atomic results.

Another useful application of the atomic experiments relates to the predictions of possible "light" bosons [105] mediating interactions in certain supersymmetric theories [106]. Because of the low-energy character of the atomic interactions, atomic PNC should be quite sensitive to lighter bosons [107].

8.1. Future prospects

In the case of heavy atoms improved experimental accuracy will pay off in all elements, but particularly in Cs and to a somewhat lesser extent in Tl, because of the accuracy of the atomic theory and the degree of understanding of the levels involved in these two atoms. Improved measurements of Q will yield more refined comparison of the type shown in eqs. (80), (81), (85) and (86) above. It remains to be seen whether improved experimental accuracy will allow resolution of the small ($\sim 10^{-2}$) fractional differences in PNC between hyperfine components of a transition, induced by the C_2 terms of eq. (21) [24]. The effects of C_2 terms have yet to be observed accurately.

As pointed out already, the hydrogen experiments can offer measurements of C_1 and C_2 with no uncertainties in atomic theory, and furthermore are sensitive to radiative corrections that test the essence of gauge theories at $\simeq 100\ \mathrm{GeV}/c$ momentum transfer.

The present atomic physics experiments give clear evidence for parity nonconservation with T-symmetry in atoms. The new class of experiments searching for T-violating EDM's in atoms and molecules should have far greater sensitivity than previous measurements and already have begun to yield significant results [88]. Through all of these investigations it appears that atomic physics experiments will continue to contribute useful information to our knowledge of fundamental symmetries in nature.

References

[1] T.D. Lee and C.N. Yang, Phys. Rev. 104 (1956) 254.
[2] C.S. Wu et al., Phys. Rev. 105 (1957) 1413.
[3] S.L. Glashow, Nucl. Phys. 22 (1961) 579.
[4] S. Weinberg, Phys. Rev. Lett. 19 (1967) 1264.

[5] A. Salam, in: Elementary Particle Theory, Proc. 8th Nobel Symp. (1968) p. 367.
[6] N.F. Ramsey, Phys. Reports 43 (1978) 410 and in: Atomic Physics 7, eds. D. Kleppner and F. Pipkin (Plenum, 1981) p. 65;
I.S. Altarev et al., Phys. Lett. 102B (1981) 13.
[7] P.G.H. Sandars, in: Atomic Physics 4, eds. G. zu Putlitz, E.W. Weber and A. Winnacker (Plenum, 1975) p. 71.
[8] E.N. Fortson and L. Wilets, in: Advances in Atomic and Molecular Physics, eds. B. Bederson and D.R. Bates (Academic Press, 1980) vol. 16, p. 319;
E.D. Commins and P.H. Bucksbaum, Ann. Rev. Nucl. Part. Sci. 30 (1980) 1;
L.M. Barkov, I.B. Khriplovich and M.S. Zolotorev, Phys. Rev. (Soviet Scientific Reviews Sec. A) 3 (1981) 1.
[9] Ya.B. Zel'dovich, Zh. Eksp. Theor. Fiz. 36 (1959) 964.
[10] F. Curtis-Michel, Phys. Rev. 138 (1965) B408.
[11] L.C. Bradley III and N.S. Wall, Nuovo Cimento 25 (1962) 48;
R. Poppe, Physics (Utrecht) 50 (1970) 48.
[12] F.J. Hasert et al., Phys. Lett. 46B (1973) 138.
A. Bevenuti et al., Phys. Rev. Lett. 32 (1974) 800;
B.C. Barish et al., Phys. Rev. Lett. 34 (1975) 538.
[13] C.Y. Prescott et al., Phys. Lett. 77B (1978) 347.
[14] G. Arnison et al., Phys. Lett. 122B (1983) 103;
M. Banner et al., Phys. Lett. 122B (1983) 476;
G. Arnison et al., Phys. Lett. 126B (1983) 398.
[15] M.A. Bouchiat and C.C. Bouchiat, Phys. Lett. 48B (1974) 111.
[16] D.C. Soreide and E.N. Fortson, Bull. Am. Phys. Soc. [2] 20 (1975) 491;
D.C. Soreide et al., Phys. Rev. Lett. 36 (1976) 352.
[17] I.B. Khriplovich, Pis'ma Zh. Eksp. Fiz. 20 (1974) 686, and JETP Lett. 20 (1974) 315.
[18] S. Chu, R. Conti and E.D. Commins, Phys. Lett. 60A (1977) 96.
[19] R.R. Lewis and W.L. Williams, Phys. Lett. 59 (1975) 70.
[20] E.G. Adelberger, T.A. Trainor and E.N. Fortson, Bull. Am. Phys. Soc. [2] 23 (1978) 546;
E.G. Adelberger et al., Nucl. Instrum. Methods 179 (1981) 181.
[21] R.W. Dunford, R.R. Lewis and W.L. Williams, Phys. Rev. A18 (1978) 2421.
[22] E.A. Hinds and V.W. Hughes, Phys. Lett. 67B (1977) 486.
[23] R.W. Robinett and J.L. Rosner, Phys. Rev. D25 (1982) 3036.
[24] V.N. Novikov et al., JETP 46 (1977) 420.
[25] W.J. Marciano and A. Sirlin, Phys. Rev. D27 (1983) 552;
B.W. Lynn, in: Recent Advances in Atomic Physics, ed. G. Grynberg (North-Holland, 1984);
B.W. Lynn, Ph.D. thesis, Columbia University, N.Y., 1981, unpublished.
W.J. Marciano and A.I. Sanda, Phys. Rev. D17 (1978) 1313.
[26] E.A. Hinds and P.G.H. Sandars, Phys. Rev. A21 (1980) 471 and 480;
P.V. Coveney and P.G.H. Sandars, J. Phys. B16 (1983) 3727.
[27] D.A. Wilkening, N.F. Ramsey and D.J. Larson, Phys. Rev. A29 (1984) 425.
[28] T.G. Vold, F.J. Raab and E.N. Fortson, Bull. Am. Phys. Soc. 27 (1982) 37 (HE2 and HE3).
[29] J.H. Christenson et al., Phys. Rev. Lett. 13 (1964) 138.
[30] A. Messiah, Quantum Mechanics, vol. 2 (Wiley, 1968) p. 569.
[31] M.A. Bouchiat and C.C. Bouchiat, J. Phys. (Paris) 35 (1974) 899.
[32] M.A. Bouchiat and C.C. Bouchiat, J. Phys. (Paris) 36 (1975) 493.
[33] M.W.S.M. Brimicombe, C.E. Loving and P.G.H. Sandars, J. Phys. B9 (1976) L237; Revised results quoted in ref. [8];
E.M. Henley and L. Wilets, Phys. Rev. A14 (1976) 1411; Revised results quoted in ref. [8].
[34] B.W. Lynn, in: 1983 Trieste Conf. on Radiative Corrections in SU2XU1, eds. B.W. Lynn and J.F. Wheater (World Scientific, Singapore, 1984);
B.W. Lynn, Nucl. Phys. B, to be published;
J.F. Wheater, Phys. Lett. 105B (1981) 483;
M. Davier, in: Proc. 21st Int. Conf. on High Energy Physics (Paris, 1982);
M. Davier, J. Phys. (Paris) 43 (1982) C3-471.
[35] E. Fermi and E. Segré, Z. Phys. 82 (1933) 729.
[36] L.M. Barkov and M.S. Zolotorev, Pis'ma Zh. Eksp. Teor. Fiz. 27 (1978) 379, and JETP Lett. 27 (1978) 357.
[37] D.V. Saskyan, I.I. Sobel'man and E.A. Yukov, Pis'ma Zh. Eksp. Teor. Fiz. (1979), and JETP Lett. 29 (1979) 258.
[38] G.J. Roberts et al., J. Phys. B13 (1980) 1389.
[39] S.L. Carter and H.P. Kelly, Phys. Rev. Lett. 42 (1979) 966.
[40] P.G.H. Sandars, Phys. Scr. 21 (1980) 284.
[41] J. Hiller et al., Ann. Phys. (N.Y.) 127 (1980) 149.
[42] P.G.H. Sandars, J. Phys. B10 (1977) 2983.

[43] A.M. Märtensson, E.M. Henley and L. Wilets, Phys. Rev. A24 (1981) 308.
[44] M.J. Harris, C.E. Loving and P.G.H. Sandars, J. Phys. B11 (1978) L749.
[45] See L. Wilets, in: Neutrino-78, ed. E. Fowler (Purdue, 1978) p. 437.
[46] V.N. Novikov, O.P. Sushkov and I.B. Khriplovich, Zh. Eksp. Teor. Fiz. 71 (1976) 1665, and JETP 44 (1976) 872.
[47] P.G.H. Sandars, private communication, 1982, and in: Proc. 7th Vavilov Conf. Novosibirsk, ed. S.G. Rautian (1981).
[48] H. Namizake, IEEE J. Quantum Electron. 1 (1975) 427.
[49] A. Aiki et al., Appl. Phys. Lett. 30 (1977) 795.
[50] P.E.G. Baird et al. and E.N. Fortson et al., Nature (London) 264 (1976) 528.
[51] L.L. Lewis et al., Phys. Rev. Lett. 39 (1977) 795.
[52] G.A. Apperson, Ph.D. thesis, University of Washington, Seattle, 1979.
[53] J.H. Hollister et al., Phys. Rev. Lett. 46 (1981) 643.
[54] P.E.G. Baird et al., private communication, 1981.
[55] P.E.G. Baird et al., Phys. Rev. Lett. 39 (1977) 798.
[56] P.E.G. Baird et al., Proc. 7th Vavilov Conf. Novosibirsk, ed. S.G. Rautian (1981) p. 22.
[57] L.M. Barkov and M.S. Zolotorev, Pis'ma Zh. Eksp. Teor. Fiz. 28 (1978).
[58] L.M. Barkov, I.B. Khriplovich and M.S. Zolotorev, Comments At. Mol. Phys. 8 (1979) 79.
[59] Yu. V. Bogdanov et al., JETP Lett. 31 (1980) 214 and 522;
G.N. Birich, Yu. V. Bogdanov, S.I. Kanorskii, I.I. Sobelman, V.N. Sorokin, I.I. Struk and E.A. Yukov, Preprint No. 136, P.N. Lebedev Physical Institute, Moscow (1984).
[60] J.J. Hsieh, Appl. Phys. Lett. 28 (1976) 283;
H. Nishi et al., Appl. Phys. Lett. 35 (1979) 232.
[61] T.P. Emmons, J.M. Reeves and E.N. Fortson, Phys. Rev. Lett. 51 (1983) 2089.
[62] J. Hoffnagle et al., Phys. Lett. 85A (1981) 143.
[63] J. Hoffnagle, V.L. Telegdi and A. Weis, Phys. Lett. 86A (1981) 457.
[64] S. Gilbert, R. Watts and C. Wieman, Phys. Rev. A27 (1983) 581, and Phys. Rev. A29 (1984) 137.
[65] D.V. Neuffer and E. Commins, Phys. Rev. A16 (1977) 844.
[66] O.P. Sushkov, V.V. Flambaum and I.B. Khriplovich, Zh. Eksp. Teor. Fiz. 24 (1976) 502 (JETP Lett. 24 (1976) 461).
[67] B.P. Das et al., Phys. Rev. Lett. 49 (1982) 32.
[68] E.D. Commins, in: Atomic Physics 7, eds. D. Kleppner and F. Pipkin (Plenum, 1981) p. 121.
[69] C.E. Loving and P.G.H. Sandars, J. Phys. B8 (1975) L336.
[70] C. Bouchiat, C.A. Piketty and D. Pignon, Nucl. Phys. B221 (1983) 68;
C. Bouchiat, in: Atomic Physics 7, eds. D. Kleppner and F. Pipkin (Plenum, 1981);
B.P. Das et al., to be published.
[71] M.A. Bouchiat, J. Guena, L. Pottier and L. Hunter, Phys. Lett. 134B (1984) 463, and references therein.
[72] M.A. Bouchiat, J. Guena, L. Hunter and L. Pottier, Phys. Lett. 117B (1982) 358.
[73] M.A. Bouchiat and L. Pottier, J. Phys. Lett. (Paris) 37 (1976) L79.
[74] M.A. Bouchiat, J. Guena and L. Pottier, J. Phys. Lett. (Paris) 41 (1980) L299.
[75] R. Conti, P. Bucksbaum, S. Chu, E. Commins and L. Hunter, Phys. Rev. Lett. 42 (1979) 343.
[76] E. Commins, P. Bucksbaum and L. Hunter, Phys. Rev. Lett. 46 (1981) 640;
P.H. Bucksbaum, E.D. Commins and L.R. Hunter, Phys. Rev. D24 (1981) 1134.
[77] P. Drell and E. Commins, Phys. Rev. Lett. 53 (1984) 968.
[78] E.M. Henley, private communication, 1983.
[79] E.A. Hinds, Phys. Rev. Lett. 44 (1980) 374.
[80] K.C. Harvey, J. Appl. Phys. 53 (1982) 3383.
[81] R. Casella, Phys. Rev. Lett. 22 (1969) 554.
[82] I.B. Khriplovich, JETP 44 (1976) 25.
[83] G. Feinberg, Trans. N.Y. Acad. Sci. 38 (1977) 26.
[84] C. Bouchiat, Phys. Lett. 57B (1975) 184.
[85] E.A. Hinds, C.E. Loving and P.G.H. Sandars, Phys. Lett. 62B (1976) 97.
[86] A.M. Märtensson-Pendrill, private communication, 1982.
[87] P.G.H. Sandars, Phys. Rev. Lett. 19 (1967) 1396.
[88] T.G. Vold, F.J. Raab, B. Heckel and E.N. Fortson, Phys. Rev. Lett. 52 (1984) 2229;
C.H. Volk et al., Phys. Rev. A21 (1980) 1549.
[89] M.C. Weisskopf et al., Phys. Rev. Lett. 21 (1968) 1645.
[90] M.A. Player and P.G.H. Sandars, J. Phys. B3 (1970) 1620.
[91] L. Wolfenstein, Phys. Rev. Lett. 13 (1964) 562.
[92] M. Kobayashi and K. Maskawa, Prog. Theor. Phys. 49 (1973) 652.
[93] T.D. Lee, Phys. Reports 9C (1974) 148;
S. Weinberg, Phys. Rev. Lett. 37 (1976) 657.

[94] R.N. Mohapatra, Phys. Rev. D6 (1972) 2023.
[95] G. 't Hooft, Phys. Rev. Lett. 37 (1976) 8, and Phys. Rev. D14 (1976) 3432;
R. Jackiw and C. Rebbi, Phys. Rev. Lett. 37 (1976) 172;
C.G. Callan, R.F. Dashen and D.J. Gross, Phys. Lett. 63B (1976) 334.
[96] J. Ellis, M.K. Gaillard, D.V. Nanopoulos and S. Rudaz, Phys. Lett. 99B (1981) 101.
[97] S. Barr, private communication, 1983;
W. Haxton, E.M. Henley and L. Wilets, private communication, 1983.
[98] L.I. Schiff, Phys. Rev. 132 (1963) 2194.
[99] D. MacArthur and F. Calaprice, private communication, 1983;
D.W. MacArthur, Ph.D. thesis, Princeton University, 1983.
[100] M.B. Gavela and H. Georgi, private communication, 1983.
[101] P.G.H. Sandars, Phys. Lett. 14 (1965) 194.
[102] P.A. Ekstrom, Bull. Am. Phys. Soc. 16 (1971) 849;
E.S. Ensberg, Phys. Rev. 153 (1967) 36.
[103] E.N. Fortson, Bull. Am. Phys. Soc. 28 (1983) 1321.
[104] P.Q. Hung and J.J. Sakurai, Phys. Lett. 88B (1979) 91.
[105] P. Fayet, Phys. Lett. 84B (1979) 416.
[106] P. Fayet, Phys. Lett. 69B (1977) 489.
[107] C. Bouchiat and C.A. Piketty, Phys. Lett. 128B (1983) 73.